RSC Advances

ROYAL SOCIETY OF CHEMISTRY

www.rsc.org/advances

Table of Contents Graphic:

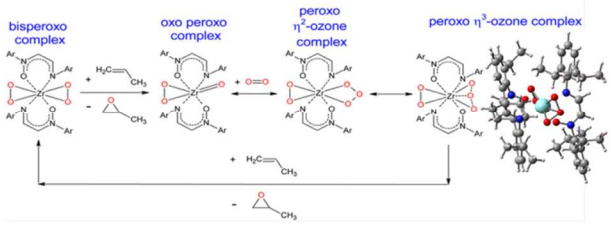

An unprecedented catalytic route for selective oxidation is designed that passes through η^3-ozone intermediates and uses molecular oxygen as the oxidant without requiring a coreductant. DFT-computed reaction cycles identify a new catalyst type with a computed overall activation energy of ~28.3 kcal/mol for direct propene epoxidation—the lowest reported for any catalyst to date.

Selective Oxidation Passing through η^3-Ozone Intermediates: Applications to Direct Propene Epoxidation Using Molecular Oxygen Oxidant

Thomas A. Manz* and Bo Yang

Chemical Engineering Department, New Mexico State University, Las Cruces, NM 88003-8001.

*corresponding author email: tmanz@nmsu.edu

Abstract:

Computations were used to design a new catalytic route for selective oxidation using molecular oxygen as the oxidant without requiring a coreductant. Formation of η^3-ozone intermediates is a key feature. Key steps in the catalytic cycle are: (a) the η^3-ozone group adds an O atom to substrate (e.g., propene) to form substrate oxide (e.g., propylene oxide) plus a peroxo or adsorbed O_2 group, (b) the peroxo or adsorbed O_2 group adds an O atom to substrate to form substrate oxide plus an oxo group, (c) an oxygen molecule adds to the oxo group to generate an η^2-ozone group, and (d) the η^2-ozone group rearranges to regenerate the η^3-ozone group. Our Density Functional Theory (DFT) calculations reveal the first instances of this catalytic cycle for any material. We expect this catalytic cycle could be used to selectively oxidize a variety of substrates. As a commercially important example, we focus on applications to direct propene epoxidation. Existing commercial manufacture of propylene oxide uses propene oxidation with one or more co-reactants and produces co-products/by-products. Direct propene epoxidation (i.e., without co-reactants) is a potentially greener process with economic and environmental benefits due to eliminating or reducing co-product/by-product formation. The grand challenge is to identify catalysts that can efficiently activate an oxygen molecule and sequentially add the resulting O atoms to two propene molecules in a catalytic cycle. We use DFT to identify and study several catalysts. Our computations introduce two new classes of Zr organometallic complexes that have dinitrone and imine-nitrone based bis-bidentate ligands, respectively. For these and bis-diimine ligated Zr complexes, we study the stability of different catalyst forms as a function of oxygen chemical potential and compute complete catalytic cycles with transition states. A new homogeneous Zr catalyst is designed with a computed enthalpy energetic span (i.e., apparent activation energy for the entire catalytic cycle) of ~28.3 kcal/mol—the lowest reported for any direct propene epoxidation catalyst to date. We propose an electrochemical cell process for assembling these catalysts and a preliminary chemical process flow diagram for direct propene epoxidation.

keywords: selective oxidation, propene epoxidation, oxygen transfer reactions, propylene oxide, propylene glycol, non-innocent ligands, redox-active ligands, Zr organometallic complexes, peroxide complexes

1. Introduction

Propylene oxide [CAS registry 75-56-9] is one of the top chemicals produced worldwide by mass and ranked as the 35th most produced chemical in 1994.[1] About ten billion pounds are currently produced annually.[2] Propylene oxide is a key intermediate in the production of many chemical products including polyether polyols (used to make polyethers and polyurethanes), propylene glycols (used to make unsaturated polyester resins and industrial fluids), and propylene glycol ethers (used to make paints).[2] The relative quantity of these uses is shown in Figure 1.

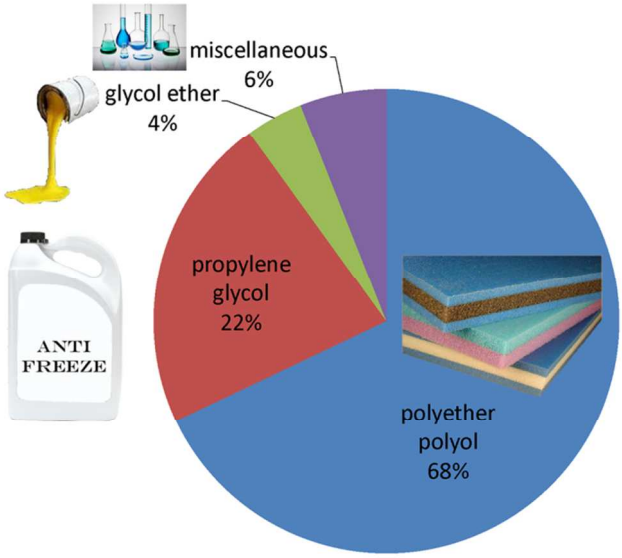

Figure 1: Common propylene oxide uses

Propylene oxide can be reacted with water to give propylene glycols that are used to produce unsaturated polyester resins and industrial fluids.[3, 4] Both monoethylene glycol and monopropylene glycol can be used as: (a) antifreeze fluids in automobiles, (b) anti-icer and de-icing fluids for airplanes and airport runways, and (c) coolant fluids and solvents.[5, 6] Monoethylene glycol and monopropylene glycol are produced by the hydration of ethylene oxide and propylene oxide, respectively. Monoethylene glycol is extremely toxic and acute exposure is sometimes fatal.[7, 8] Monopropylene glycol is generally regarded as safe, but large intravenous doses given over a short period of time can be toxic.[9] For the safety of consumers, it would generally be desirable to replace monoethylene glycol with monopropylene glycol in these applications. However, monopropylene glycol is almost twice as expensive as monopropylene glycol on a molar basis, as shown in Table 1. While this is partly due to the higher cost of propylene than ethylene (see Table 1), the main reason is the greater difficulty of manufacturing propylene oxide than ethylene oxide. Ethylene oxide can be efficiently manufactured on a commercial scale by the direct oxidation of ethylene with molecular oxygen over silver catalysts.[10-12] However, passing propylene and molecular oxygen over similar catalysts produces many unwanted by-products.[12-15]

Table 1: Boiling points, 2011-2012 chemical prices, and approximate production rank

	normal boiling point[a] (°C)	recent price $/lb.[b]	molar mass g/mol	molar price $/kmol	1994 production rank[c]
ethylene	-103.7	0.46	28.05	28	4
propylene	-47.6	0.52	42.08	48	7
ethylene oxide	10.7	0.60	44.05	58	26
propylene oxide	34	0.95	58.08	122	35
monethylene glycol	197.3	0.50	58.08	68	30
monopropylene glycol	188.2	0.75	62.07	126	>50

[a] The normal boiling point of a chemical is the temperature for which the pure liquid exerts a vapor pressure of 1 atmosphere. [b] ICIS Chemical Business, ICIS.com. [c] From reference [1].

As shown in Figure 2, propylene oxide is currently manufactured by a variety of processes.[2, 12] In chlorohydrin processes, propene is reacted with chlorine gas to produce a propene-chloronium complex that is hydrolyzed to form chloro-propanol that is subsequently reacted with $Ca(OH)_2$ (or NaOH) to produce propylene oxide plus $CaCl_2$ (or 2NaCl).[2, 12] Although yields are good, chlorinated by-products and brine are produced in this process.[2, 12] Another common commercial process involves the formation of organic hydroperoxides generated by catalytic oxidation in air or oxygen.[2] In addition to propylene oxide, this process produces a co-product like methyl *tert*-butyl ether (MTBE) or styrene.[2] The economics of this process are strongly influenced by the co-product's market value. A variation of the hydroperoxide process has been developed that avoids co-products.[12] In this variation, cumene is converted to its hydroperoxide which oxidizes propene to propylene oxide and forms an alcohol that is passed over a catalyst to regenerate cumene.[12] This process gives high yield and selectivity to propylene oxide,[12] but consumes one mole of H_2 (to regenerate cumene) for each mole of propylene oxide produced. Other commercial processes use hydrogen peroxide (H_2O_2) as an intermediate oxidant.[2, 12, 16] Transporting H_2O_2 for this process is uneconomical, so it must be generated on site.[17] Theoretically, this process would only produce water as a co-product.[17] The required H_2O_2 is generated by the reaction $H_2 + O_2 \rightarrow H_2O_2$ over a catalyst or via the anthraquinone process.[17] Although high conversion and selectivity to propylene oxide can be obtained, this process has the disadvantage of consuming at least one mole of H_2 for every mole of propylene oxide produced. There is continuing interest to improve the economic and environmental aspects of propylene oxide manufacture.[18-21]

Cumene and hydrogen peroxide routes

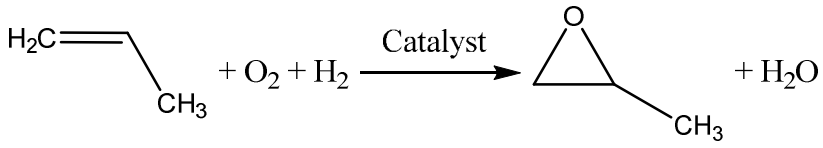

Chlorohydrin routes

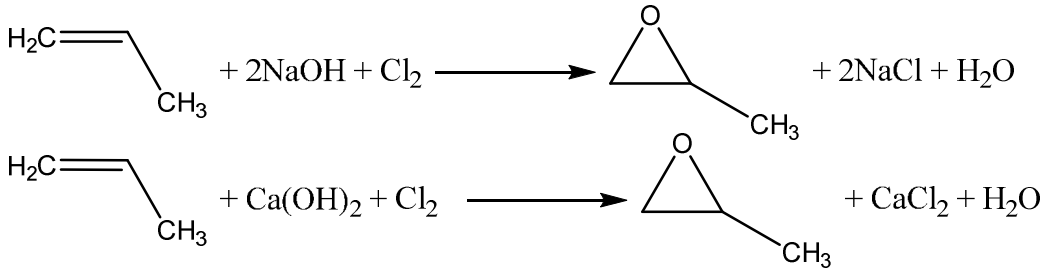

Coproduct routes

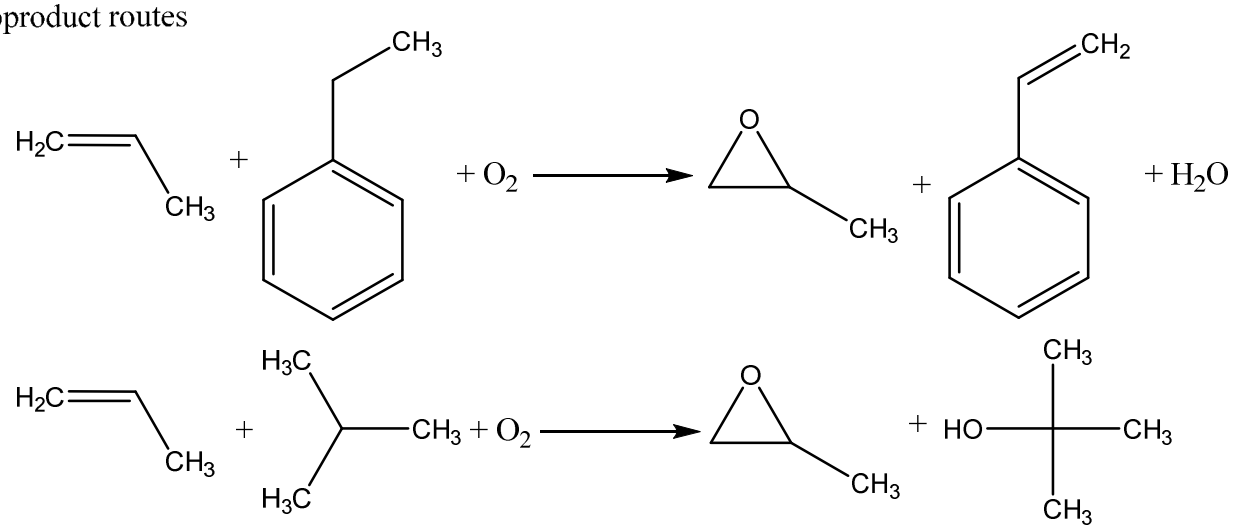

Figure 2: Current routes for large-scale propylene oxide manufacture

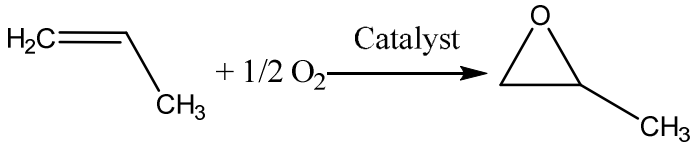

Figure 3: Direct epoxidation of propene using molecular oxygen oxidant

All of these commercial processes fall short of the ideal in which propene and O_2 would be reacted over a catalyst to directly produce propylene oxide without the need for H_2 addition or co-product formation. The direct oxidation route is shown in Figure 3. According to the 2012 edition of Ullman's Encyclopedia of Chemical Technology, "There is no direct oxidation process

for producing propylene oxide that is close to commercialization."[2] "The breakthrough in direct oxidation of propene to propylene oxide has not yet been achieved."[2] Despite vigorous research using a variety of catalyst architectures, the combination of high selectivity and high conversion to propylene oxide has been elusive.[13, 14, 22-32] The principle challenge is to develop a catalyst that efficiently catalyzes the direct oxidation of propene to propylene oxide using molecular oxygen as oxidant. By "efficiently catalyzes" we mean the catalyst should simultaneously produce a high conversion and high selectivity to propylene oxide with high catalyst stability. This catalyst should minimize the amount of co-reactants, co-products, and by-products.

Epoxide synthesis can be accomplished using organometallic oxygen transfer catalysts. These catalysts typically contain a Co, Cr, Fe, La, Mn, Mo, Ni, Pd, Re, Ru, Ti, V, or W central metal atom bound to O and/or N containing polydentate ligands and use iodosylbenzene, H_2O_2, organic peroxides, NaClO (i.e., common bleach), Oxone, or other compounds as the terminal oxidant.[33-38] DFT studies have investigated the epoxidation mechanism for these types of catalysts.[39-44] If a high cost oxidant is used, the process is economically limited to expensive epoxides or to small-scale laboratory syntheses. Replacing these oxidants with molecular oxygen could potentially save costs. However, few of these catalysts can activate molecular oxygen and nearly all of the ones that do require a reductant.[36, 45] When a reductant is used, one of the oxygen atoms from the O_2 molecule is used to form a by-product/co-product and the other oxygen atom is transferred to an alkene to form the desired epoxide.[36, 45] In summary, the existing organometallic oxygen transfer catalysts are not efficient for direct propene epoxidation.

In this article, we study the three catalyst architectures shown in Figure 4. Each of these catalysts contains a Zr metal atom bound to two bidentate ligands with (a) N(Ar)-CH-CH-N(Ar), (b) N(Ar)-CH-CH-N(Ar)-O, or (c) O-N(Ar)-CH-CH-N(Ar)-O [Ar = $-C_6H_3$-2,6-$^iPr_2$] linkages in the ligand backbone. These are representative of classes of Zr organometallic complexes having (a) diimine, (b) imine-nitrone, and (c) dinitrone based bis-bidentate ligands, respectively. In these images, the π-electrons are illustrated as delocalized dashed bonds to represent the ability of these π-electrons to move amongst the atom pairs as the catalyst form changes. The Zr bisperoxo complex shown in Figure 4 (a) has been previously synthesized by Stanciu et al.[46] To the best of our knowledge, the imine-nitrone and dinitrone based catalyst systems, ligands, and catalyst classes depicted in Figure 4 (b) and (c) are brand new. For convenience, we hereafter use the notation M'' to represent the Zr catalyst containing the NCCN linkage, M' to represent the Zr catalyst containing the NCCNO linkage, and M to represent the Zr catalyst containing the ONCCNO linkage. The bisperoxo forms of these catalysts are denoted M''$(O_2)_2$, M'$(O_2)_2$, and M$(O_2)_2$, respectively.

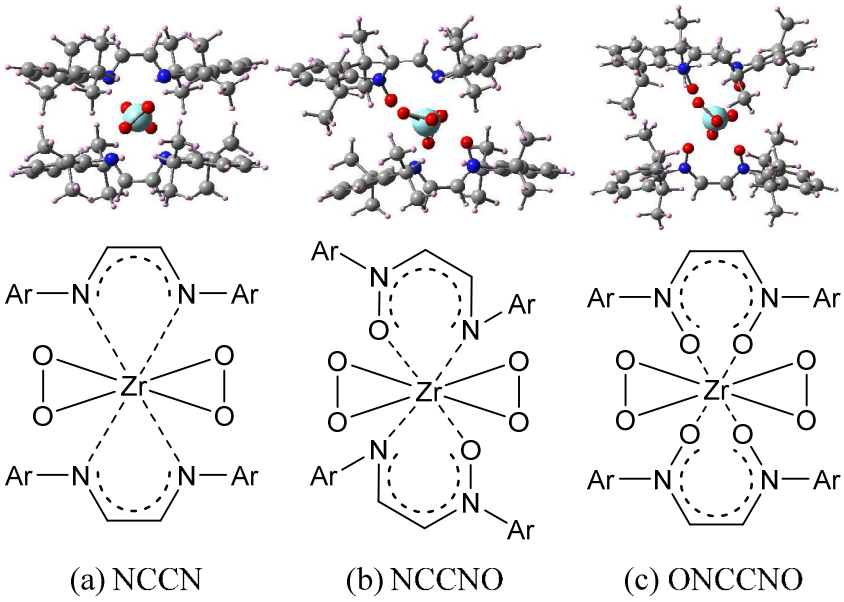

Figure 4: The (a) NCCN, (b) NCCNO, and (c) ONCCNO catalyst architectures as representative members of Zr organometallic complexes containing (a) diimine, (b) imine-nitrone, and (c) dinitrone based bidentate ligands, respectively. The spiro bisperoxo forms are illustrated with Ar = C_6H_3-2,6-$^{i}Pr_2$.

These catalysts were selected using chemical insights, DFT calculations, and trial and error. Most organometallic complexes previously used for alkene epoxidation (with a variety of oxidants) contain a metal atom bound to several O (and sometimes N) atoms and involve metal-oxo, metal-peroxo, metal-hydroperoxo, or metal-alkoperoxo intermediates.[33-36, 39-44] This observation motivated us to study peroxo-containing complexes as potential catalysts for propene epoxidation. The choice of complexes with redox non-innocent ligands was motivated by our belief that these ligands would stabilize the system's energy by absorbing and releasing electrons to the catalytic center as needed. Several key factors led to the particular selection of the M''$(O_2)_2$ system for this study: (a) it is stable in the presence of air and moisture,[46] (b) it is a bisperoxo complex with redox non-innocent ligands,[46] and (c) one of us has previously studied net atomic charges, geometric parameters, and effective bond orders for its bare complex and bisperoxo forms.[47-49] However, this M''$(O_2)_2$ complex has not previously been shown active for any reaction except O_2 desorption.[46] Our DFT computations showed a peroxo η^2-ozone intermediate M''$(O_2)(O_3)_{(a)}$ can be formed. Initially, we tried to transfer one O atom from M''$(O_2)(O_3)_{(a)}$ to propene to produce propylene oxide plus M''$(O_2)_2$. However, constrained geometry optimizations failed to locate an appropriate reaction path and transition state. During these DFT transition state searches, one O atom from the adsorbed ozone reacted with the NCCN linkage to produce the NCCNO linkage. This observation led to additional DFT calculations showing the NCCNO linkage is more stable (i.e., lower in energy) than the NCCN linkage. A key breakthrough occurred when our DFT calculations revealed a peroxo η^3-ozone intermediate M'$(O_2)(O_3)_{(b)}$ for the NCCNO ligand architecture in which all three ozone atoms are Zr bound, as

shown in Figure 5. This allowed one O atom to be easily removed by propene to generate the M'$(O_2)_2$ complex plus propylene oxide. The initial idea for the net reaction was ethylene oxide + propene → propylene oxide + ethene, where ethylene oxide would transfer an O atom to M'$(O_2)_2$ to regenerate the M'$(O_2)(O_3)_{(a)}$ complex. It soon became apparent that removal of an O atom from M'$(O_2)_2$ by propene to form an oxo peroxo complex plus propylene oxide would facilitate epoxidation using molecular oxygen as the oxidant. The corresponding direct propene epoxidation cycle was computed shortly thereafter. The existence of a catalytic cycle based on the NCCNO peroxo η^3-ozone intermediate prompted the question of whether an analogous catalytic cycle exists for an oxo η^3-ozone intermediate. Our DFT calculations confirmed this. We performed similar DFT calculations to compute catalytic cycles for the ONCCNO and NCCN ligand architectures. This briefly summarizes the choice of these three catalyst architectures.

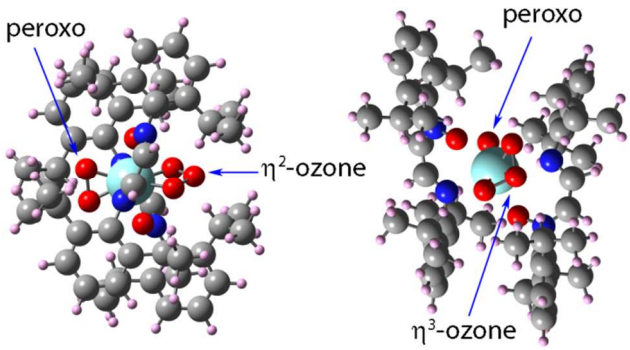

Figure 5: Different peroxo ozone complexes for the NCCNO catalyst. *Left:* peroxo η^2-ozone, *Right*: peroxo η^3- ozone.

We envision a multiphase process for developing commercially viable Group 4 organometallic complexes for the direct epoxidation of propene (and other alkenes) using molecular oxygen as the oxidant. For Phase 1, we envision (i) a series of computational chemistry calculations to identify potential catalyst structures having a low energetic span for direct epoxidation reactions and (ii) initial design of a chemical process flow diagram to identify target operating conditions (e.g., temperatures, pressures, and catalyst separation method) to use as targets when designing catalysts. For Phase 2, we envision the development of catalyst synthesis procedures and experimental tests for direct epoxidation reactivity to demonstrate experimental viability. For Phase 3, we envision modifying catalyst structures and reaction conditions to optimize catalyst reactivity, selectivity, and stability. For Phase 4, we envision a more complete process design, scale-up, and commercialization. We do not envision each phase as ending when the next phase begins. For example, we envision that Phase 1 computational screening will continue to be performed concurrently with Phases 2, 3, and 4. We envision an interactive improvement process wherein results from each phase inform activities in all of the other phases. In this article, we report some Phase 1 results.

The remainder of this article is organized as following. Section 2 summarizes the methods used to compute the energies and molecular geometries. Section 3.1 presents and discusses diagrams in which the relative energies of different catalyst forms are plotted as a

function of the oxygen chemical potential. These diagrams give valuable insights into the preferred catalyst forms under reaction conditions. Section 3.2 presents and discusses computed catalytic cycles with transition states for each of the three catalysts. Section 3.3 gives energetic spans that quantify apparent energy barriers for entire catalytic cycles. Section 3.4 describes catalyst interconversion and potential side reactions. Section 3.5 contains a structural analysis of the η^3-ozone complexes and a literature search for related peroxo and ozone complexes. Section 4 proposes an electrochemical cell process for catalyst assembly. Section 5 proposes a preliminary chemical process flow diagram that is suitable for using these types of catalysts for direct propene epoxidation. The main findings of this article, potential catalyst variations, and potential applications to selectively oxidize other substrates are summarized in Section 6.

2. Methods

DFT simulations were performed with GAUSSIAN software using the B3LYP exchange-correlation functional[50, 51] and LANL2DZ basis sets.[52] Geometries were optimized in vacuum to better than 0.005 Å for the atom displacements and 0.0025 AU for the forces. (In rare cases, we considered the geometry converged when the root mean squared force was $< 10^{-4}$ AU.) Zero point and thermochemistry data (at 298.15 Kelvin and 1 atmosphere pressure) were calculated using the harmonic approximation as implemented in Gaussian 09.[52]

Transition states were optimized using the following procedure. First, constrained optimizations were performed along potential reaction coordinates to generate initial transition state estimates. These transition state estimates were subsequently optimized using the quadratic synchronous transit (GAUSSIAN keyword QST3) or eigenmode following (GAUSSIAN keyword TS) methods. A frequency calculation was then performed. Each transition state was verified by ensuring it had exactly one imaginary frequency (within a computational tolerance of approximately 30 cm^{-1}). The imaginary frequency was animated in GaussView to verify it was along the desired reaction coordinate connecting reactants to products. Various conformations of the catalyst and different reaction pathways were considered. However, the stereochemistry of O addition to the propene molecule was not considered. Therefore, our calculations should not be used to make any stereochemical predictions. Because constrained geometry optimizations revealed addition of O_2 to the dioxo complexes did not have a regular transition state, the barrier for this reaction was determined by the singlet-triplet crossing point as described in the Electronic Supplementary Information.

The complete set of calculations described in this paper required a couple hundred thousand computational hours using LANL2DZ basis sets. Because larger basis sets increase the computational expense, repeating all the calculations with a larger basis set is infeasible at this time. However, we did optimize two of the geometries using a larger basis set to validate our computational approach. As summarized in Table 2, two geometries were optimized using 6-311++GG** basis sets for all non-metal atoms and the SDD basis set (which replaces 28 core electrons with a relativistic effective potential) for Zr. Both the B3LYP/LANL2DZ and B3LYP/6-311++G** methods gave good agreement with structural parameters from x-ray

diffraction (XRD) experiments. These results show our computational approach is reasonable. We do, however, acknowledge that all DFT calculations involve approximations arising from the choice of exchange-correlation functional and basis sets.

Table 2: Comparison of Experimental and Computed Structural Parameters for Zr complexes containing the NCCN linkage

	spiro bisperoxo complex (M''$(O_2)_2$)			**puckered bare complex (M'')**		
	XRD[a]	**B3LYP/ LANL2DZ**	**B3LYP/ 6-311++G**[b]**	**XRD[a]**	**B3LYP/ LANL2DZ**	**B3LYP/ 6-311++G**[b]**
Zr-O	2.03 – 2.04 Å	2.09 Å	2.07 Å	--	--	--
intraperoxy **O-O**	1.50 – 1.51 Å	1.54 Å	1.47 Å	--	--	--
Zr-N	2.43 – 2.45 Å	2.47 Å	2.51 Å	2.05 – 2.09 Å	2.08 – 2.13 Å	2.09 – 2.13 Å
intraperoxy **O-Zr-O**	43.3 – 43.7 °	43.3 °	41.7 °	--	--	--
N-**C-C**-N	1.47 – 1.48 Å	1.47 Å	1.47 Å	1.36 – 1.37 Å	1.38 Å	1.38 Å
N-C-C-N	1.26 – 1.27 Å	1.30 Å	1.28 Å	1.40 – 1.41 Å	1.43 Å	1.40 Å
N-Ar	1.45 – 1.46 Å	1.46 Å	1.45 Å	1.43 – 1.44 Å	1.44 – 1.45 Å	1.43 Å
intraligand **N-Zr-N**	68.5 – 68.8 °	69.7 °	68.5 °	86.8 – 87.1 °	86.1 – 86.2 °	86.4 °
intraligand **N-C-C-N** dihedral	-7.5 – -6.1 °	-5.8 °	-6.5 °	-1.0 – -0.2 °	0.7 °	0.2 °
angle between two **O_2-Zr** planes	77.7 °	81.0 °	81.5 °	--	--	--
angle between two **N**-C-C-**N**-**Zr** planes	32.0 °	30.8 °	31.3 °	93.1 °	91.2 °	90.2 °
angle between **Zr**-**N**-C-C-**N** and **Zr**-N-**C**-**C**-N planes for the same ligand	2.4 – 3.0 °	2.3 °	2.5 °	22.8 – 23.3 °	16.3 °	18.0 °

[a] Experimental data from reference [46]. [b] 6-311++G** basis sets on all non-metal atoms and SDD basis set on Zr.

3. Results and Discussion

3.1 Chemical Potential Diagrams

Using molecular oxygen as the oxidant requires two sequential O atom transfers from the catalyst to substrate molecules. To facilitate this, the catalyst should act like an oxygen reservoir that stabilizes the O atom chemical potential. Essentially, one wants the catalyst to act like an O atom "sponge" that freely accepts and releases O atoms with little change in the O atom chemical potential. To study this, the relative energies of different catalyst forms for the Zr_NCCNO, Zr_ONCCNO, and Zr_NCCN systems are plotted as a function of the O atom chemical potential in Figure 6, Figure 7, and Figure 8, respectively. These diagrams display key representative catalyst forms and do not contain an exhaustive set of all possible catalyst conformations. Additional structures are contained in the Electronic Supplementary Information. The diagrams are based on the B3LYP/LANL2DZ SCF energies.

The construction of these figures is now explained. The singlet spiro bisperoxo form was chosen as the catalyst reference state, and an O_2 molecule was chosen as the reference for the O atom chemical potential. The energy line for each catalyst form intercepts the x=0 line at the reaction energy required to generate it from the singlet spiro bisperoxo complex using O_2 as the O atom source. For example, the bare complex M' takes 81.9 kcal/mol to generate with the reaction $M'(O_2)_{2(a)} \rightarrow M' + 2O_2$. Singlet forms are shown in the left panel. The O atom chemical potential using propylene oxide as the O atom source forms the left vertical scale located at x=-15.9 and corresponds to the reaction energy $P + \frac{1}{2} O_2 \leftrightarrow PO$. The energy line for each catalyst form intercepts the PO line at the reaction energy required to generate it from the singlet spiro bisperoxo complex using PO as the O atom source. For example, the bare complex M' takes 18.1 kcal/mol to generate with the reaction $M'(O_2)_{2(a)} + 4P \rightarrow M' + 4PO$. The graph is composed of straight lines, because the relative energy of each catalyst form is a linear function of the O atom chemical potential. The slope of each of these lines is (4 – w) where w is the number of adsorbed O atoms in the catalyst form. Triplet forms are shown in the center panel with the O_2 chemical potential on the left and the PO chemical potential on the right. The right panel is a partial copy of the left panel. This allows energies of the singlet and triplet forms to be directly compared on the O_2 and PO chemical potential lines.

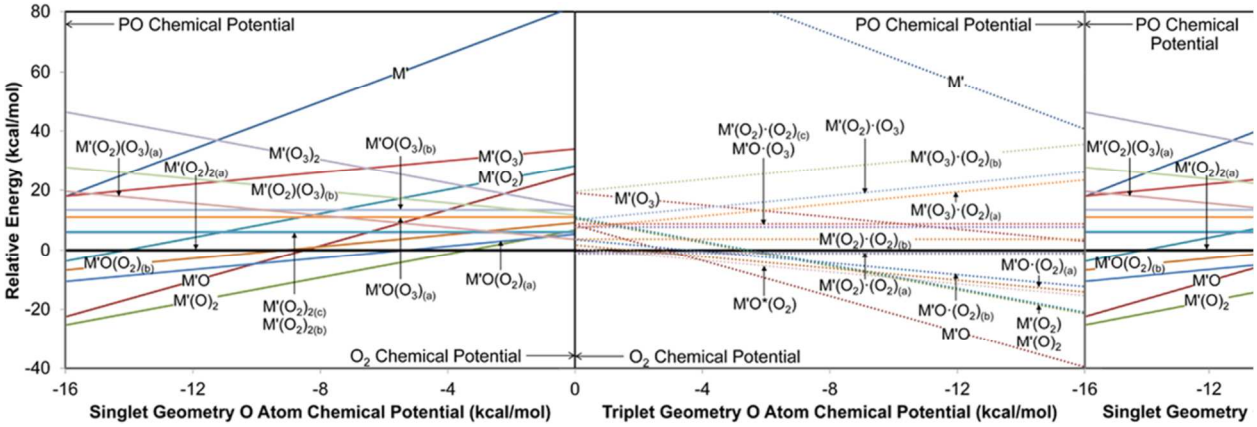

Figure 6: Chemical potential diagram for the Zr_NCCNO system. Relative energies of different catalyst forms as a function of the oxygen chemical potential. Singlet forms are displayed in the left panel; triplet forms are displayed in the center panel. The right panel is a partial copy of the left panel for easy comparison to the triplet energies. The singlet spiro bisperoxo form is the reference state. *Singlet conformations*: $M'(O_2)(O_3)(a)$ is the peroxo η^2-ozone complex; $M'(O_2)(O_3)(b)$ is the peroxo η^3-ozone complex; $M'(O_2)_2(a)$ is the spiro bisperoxo complex; $M'(O_2)_2(b)$ is the planar bisperoxo complex; $M'(O_2)_2(c)$ is the butterfly bisperoxo complex; $M'O(O_3)(a)$ is the oxo η^2-ozone complex; $M'O(O_3)(b)$ is the oxo η^3-ozone complex; $M'O(O_2)(a)$ is the butterfly oxo peroxo complex; $M'O(O_2)(b)$ is the planar oxo peroxo complex. *Triplet conformations*: $M'(O_2)\bullet(O_2)(a)$ is the spiro conformation; $M'(O_2)\bullet(O_2)(b)$ is the planar conformation; $M'(O_2)\bullet(O_2)(c)$ is the butterfly conformation; $M'(O_3)\bullet(O_2)(a)$ is the η^2-ozone complex with adsorbed O_2; $M'(O_3)\bullet(O_2)(b)$ is the η^3-ozone complex with adsorbed O_2; $M'O\bullet(O_2)(a)$ is the planar conformation; $M'O\bullet(O_2)(b)$ is the butterfly conformation.

Figure 6 for the NCCNO ligand architecture is now discussed. For O atom chemical potentials less than approximately -3 kcal/mol the triplet oxo complex, M'O, is preferred and for higher O atom chemical potentials the singlet spiro bisperoxo, $M'(O_2)_{2(a)}$, and the triplet $M'(O_2)\bullet(O_2)_{(a)}$ are preferred. The dot in structures like $M'(O_2)\bullet(O_2)_{(a)}$ precedes a weakly bound species (e.g., O_2), wherein the O-O bond length is similar to the molecular form (~1.4 Å) not a peroxo form (~1.5 Å). An extremely weakly bound O_2 group is indicated by an asterisk (e.g., $M'O^*(O_2)$). Near the chemical potential of O_2, the relative energies for major catalyst forms having 1, 2, 3, 4, 5, and 6 adsorbed O atoms are within a 30 kcal/mol window. Accordingly, this catalyst should be an excellent O atom sponge for adsorbing and releasing O atoms. The bare complex M' should have a negligible role under oxygenated reaction conditions, because it has a high relative energy (81.9 kcal/mol) near the chemical potential of O_2.

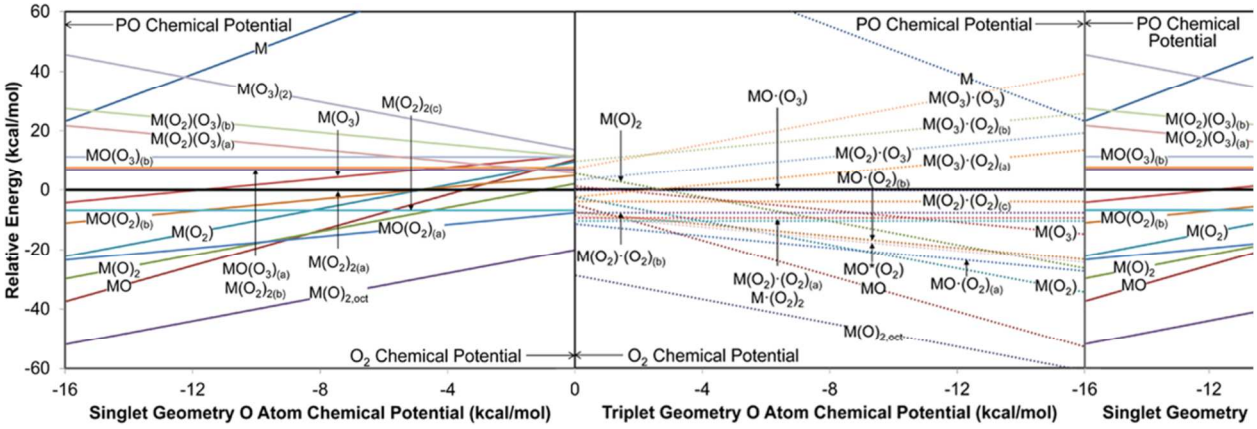

Figure 7: Chemical potential diagram for the Zr_ONCCNO system. Relative energies of different catalyst forms as a function of the oxygen chemical potential. Singlet forms are displayed in the left panel; triplet forms are displayed in the center panel. The right panel is a partial copy of the left panel for easy comparison to the triplet energies. The singlet spiro bisperoxo form is the reference state. *Singlet conformations*: $M(O_2)(O_3)(a)$ is the peroxo η^2-ozone complex; $M(O_2)(O_3)(b)$ is the peroxo η^3-ozone complex; $M(O_2)_2(a)$ is the spiro bisperoxo complex; $M(O_2)_2(b)$ is the planar bisperoxo complex; $M(O_2)_2(c)$ is the butterfly bisperoxo complex; $MO(O_3)(a)$ is the oxo η^2-ozone complex; $MO(O_3)(b)$ is the oxo η^3-ozone complex; $M(O)_{2,oct}$ is the octahedral complex; $MO(O_2)(a)$ is the butterfly oxo peroxo complex; $MO(O_2)(b)$ is the planar oxo peroxo complex. *Triplet conformations*: $M(O)_{2,oct}$ is the octahedral complex; $M(O_2)\bullet(O_2)(a)$ is the butterfly conformation; $M(O_2)\bullet(O_2)(b)$ is the spiro conformation; $M(O_2)\bullet(O_2)(c)$ is the planar conformation; $M(O_3)\bullet(O_2)(a)$ is the η^2-ozone complex with adsorbed O_2; $M(O_3)\bullet(O_2)(b)$ is the η^3-ozone complex with adsorbed O_2; $MO\bullet(O_2)(a)$ is the butterfly conformation; $MO\bullet(O_2)(b)$ is the planar conformation.

Figure 7 for the ONCCNO ligand architecture is now discussed. As shown in Figure 9, this catalyst exhibits three major bisperoxo bonding motifs: spiro, planar, and butterfly. The spiro bisperoxo complex has a corkscrew-like bonding motif in which the two peroxo groups are rotated almost perpendicular to each other. The planar bisperoxo complex has two nearly co-planar peroxo groups. In the butterfly bisperoxo complex, the ligands sit on one side of the catalyst and the two peroxo groups are lifted up like wings on the other side of the catalyst.

Among these bisperoxo complexes, the butterfly conformation has the lowest energy. The octahedral-like dioxo conformation, $M(O)_{2,oct}$, is the preferred form across the entire range of O atom chemical potentials. The triplet form of $M(O)_{2,oct}$ is slightly lower in energy than the singlet form. As shown in Figure 14 (singlet $M(O)_{2,oct}$), one of the dioxo atoms is quasi-bonded to a carbon from the ligand in this octahedral-like complex. The bare complex M of this catalyst is relatively unstable due to its high energy.

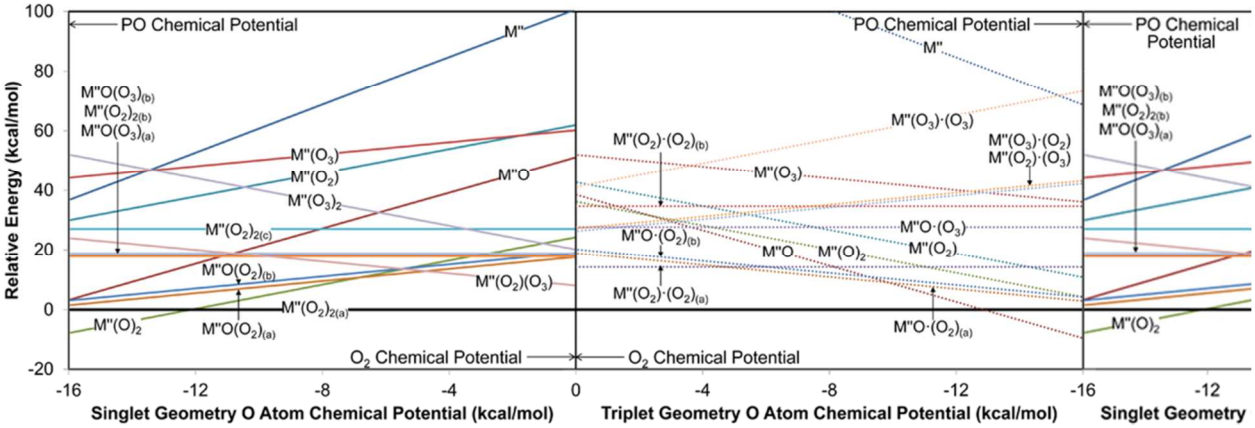

Figure 8: Chemical potential diagram for the Zr_NCCN system. Relative energies of different catalyst forms as a function of the oxygen chemical potential. Singlet forms are displayed in the left panel; triplet forms are displayed in the center panel. The right panel is a partial copy of the left panel for easy comparison to the triplet energies. The singlet spiro bisperoxo form is the reference state. *Singlet conformations*: M"O(O_3)(a) is the oxo η^2-ozone complex; M"O(O_3)(b) is the oxo η^3-ozone complex; M"(O_2)$_2$(a) is the spiro bisperoxo complex; M"(O_2)$_2$(b) is the planar bisperoxo complex; M"(O_2)$_2$(c) is the butterfly bisperoxo complex; M"O(O_2)(a) is the planar oxo peroxo complex; M"O(O_2)(b) is the butterfly oxo peroxo complex. *Triplet conformations*: M"(O_2)•(O_2)(a) is the spiro conformation; M"(O_2)•(O_2)(b) is the butterfly conformation; M"O•(O_2)(a) is the planar conformation; M"O•(O_2)(b) is the butterfly conformation.

Figure 8 for the NCCN ligand architecture is now discussed. The spiro bisperoxo complex is the preferred catalyst form for O atom chemical potentials > -13 kcal/mol. The different forms of this catalyst differ widely in energy, making it a poorer O atom sponge than the NCCNO and ONCCNO ligand architectures. A constrained geometry search (Fig. S4) showed this system does not form a peroxo η^3-ozone complex. The bare complex M" has a puckered geometry in which the N-C=C-N groups are twisted towards the Zr metal to allow weak π-bonding between the Zr metal and the C=C groups.[46] In the presence of oxygen, the bare complex is unstable relative to oxygenated catalyst forms.

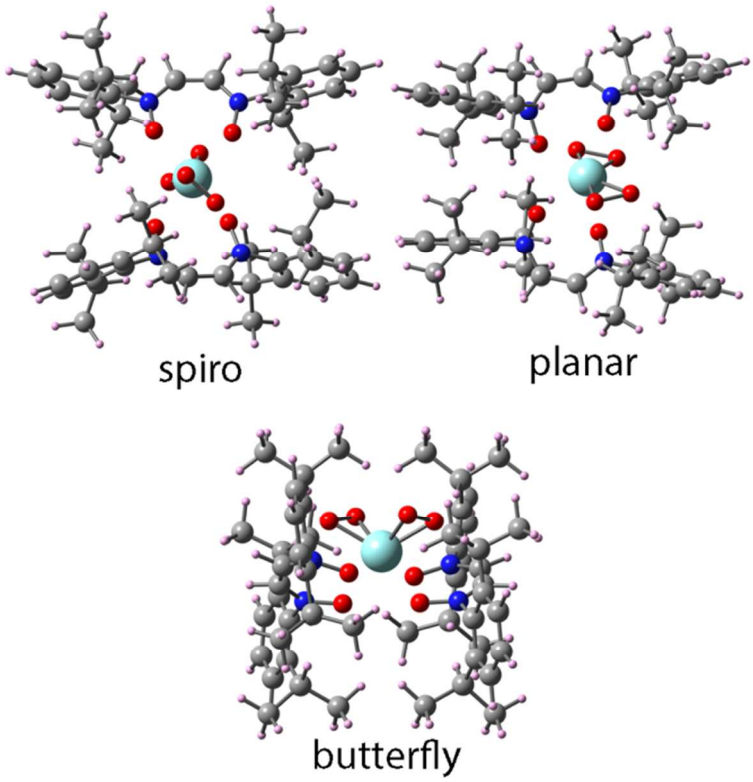

Figure 9: Different bisperoxo bonding motifs for the ONCCNO ligand architecture.

Atomic spin moments (ASMs) were computed to better understand the distribution of spin density among atoms in the triplet states. These were computed using the Density Derived Electrostatic and Chemical method.[48, 53] Table 3 summarizes the results by adding the ASMs in different parts of the structure. For all structures, the combined ASMs sum to 2.00, representing the two unpaired electrons. As shown in Table 3, only the bare complexes have a large ASM for the Zr metal center. Strongly adsorbed oxygen atoms have a large ASM in the dioxo complexes, and small ASMs in the other structures. Weakly adsorbed oxygen atoms (i.e., weakly adsorbed O_2 or O_3 groups) have large ASMs in all structures containing them. Ligand 1 was arbitrarily designated as the ligand having the largest ASMs for nitrogen atoms. For all of the triplet structures in Table 3, the two nitrogen atoms in ligand 1 had an ASM sum of 0.29–0.59. Some of the structures had appreciable spin located on ligand 2, while others did not. For example, the oxo (MO, M'O, M"O), peroxo ($M(O_2)$, $M'(O_2)$, $M"(O_2)$), and ozone ($M(O_3)$, $M'(O_3)$, $M"(O_3)$) complexes had large spin magnitude on ligand 2.

Table 3: Assigned Spin Magnetic Moments

species	Zr	non-ligand oxygens		nitrogens		other atoms
		strongly adsorbed	weakly adsorbed	ligand 1	ligand 2	
M"	0.9122	—	—	0.5428	-0.0095	0.5545
M"O	0.0088	0.0673	—	0.5599	0.4983	0.8657
$M"(O)_2$	-0.1168	1.1392	—	0.5390	0.0186	0.4200
$M"(O_2)$	0.1005	0.0228	—	0.5251	0.5250	0.8266
$M"O·(O_2)_{(a)}$	-0.0101	0.0311	1.0113	0.5626	0.0013	0.4038
$M"O·(O_2)_{(b)}$	-0.0240	0.0451	1.0075	0.5630	0.0033	0.4051
$M"(O_3)$	0.1231	0.0595	—	0.5025	0.5025	0.8124
$M"(O_2)·(O_2)_{(a)}$	-0.0149	0.0300	1.0166	0.5680	-0.0015	0.4018
$M"(O_2)·(O_2)_{(b)}$	0.0419	0.0257	1.0107	0.5006	0.0175	0.4036
$M"O·(O_3)$	0.0059	0.0478	0.9935	0.5503	0.0036	0.3989
$M"(O_3)·(O_2)$	0.0009	0.0400	1.0184	0.5458	0.0010	0.3939
$M"(O_2)·(O_3)$	0.0066	0.0423	0.9934	0.5612	0.0052	0.3913
$M"(O_3)·(O_3)$	0.0063	0.0510	0.9864	0.5557	0.0093	0.3913
M'	0.8788	—	—	0.4345	0.1761	0.5106
M'O	-0.0065	0.0405	—	0.5838	0.5822	0.8000
$M'(O)_2$	-0.1062	1.1097	—	0.5460	0.0190	0.4315
$M'(O_2)$	0.0015	0.0142	—	0.5846	0.5844	0.8153
$M'O·(O_2)_{(a)}$	-0.0231	0.0080	1.0040	0.5789	-0.0009	0.4331
$M'O·(O_2)_{(b)}$	-0.0248	0.0249	1.0062	0.5857	0.0059	0.4021
$M'O*(O_2)$	-0.0082	0.0153	1.3045	0.5826	-0.1966	0.3024
$M'(O_3)$	0.0064	0.0251	—	0.5684	0.5681	0.8320
$M'(O_2)·(O_2)_{(a)}$	-0.0269	0.0103	1.0156	0.5625	-0.0028	0.4413
$M'(O_2)·(O_2)_{(b)}$	-0.0137	0.0150	1.0097	0.5643	-0.0002	0.4249
$M'(O_2)·(O_2)_{(c)}$	-0.0348	0.1040	0.9637	0.5776	-0.0180	0.4075
$M'O·(O_3)$	-0.0065	0.0227	0.9873	0.5803	0.0005	0.4157
$M'(O_3)·(O_2)_{(a)}$	-0.0160	-0.0087	1.0017	0.5516	0.0179	0.4535
$M'(O_2)·(O_3)$	0.0039	0.0201	0.9821	0.5688	0.0004	0.4247
$M'(O_3)·(O_2)_{(b)}$	-0.0171	0.0092	0.9838	0.5774	0.0052	0.4415
M	0.9565	—	—	0.2904	0.2903	0.4628
MO	0.0082	0.0194	—	0.5506	0.5320	0.8898
$M(O)_2$	-0.0916	1.0930	—	0.5718	-0.0299	0.4567
$M(O)_{2,oct}$	0.0040	0.0215	—	0.5470	0.4624	0.9651
$M(O_2)$	0.0359	0.0055	—	0.5505	0.5504	0.8577
$MO·(O_2)_{(b)}$	-0.0115	0.0174	1.0118	0.5352	-0.0024	0.4495
$MO·(O_2)_{(a)}$	-0.0145	0.0163	1.0136	0.5319	-0.0468	0.4995
$MO*(O_2)$	-0.0028	0.0026	1.8992	0.5326	-0.5008	0.0692
$M(O_3)$	0.0449	0.0210	—	0.5425	0.5425	0.8491
$M(O_2)·(O_2)_{(b)}$	0.0025	-0.0064	1.0141	0.4542	0.0897	0.4459
$M·(O_2)_2$	-0.0518	0.0000	2.0206	0.5307	-0.5266	0.0271
$M(O_2)·(O_2)_{(c)}$	-0.0037	-0.0007	1.0110	0.5273	-0.0028	0.4689
$M(O_2)·(O_2)_{(a)}$	0.0013	0.0201	1.0025	0.4859	0.0546	0.4356
$MO·(O_3)$	0.0110	0.0144	0.9782	0.5316	0.0036	0.4612
$M(O_3)·(O_2)_{(a)}$	0.0203	-0.1346	1.0365	0.3062	0.3040	0.4676
$M(O_2)·(O_3)$	0.0122	0.0323	0.9874	0.5210	0.0115	0.4356
$M(O_3)·(O_2)_{(b)}$	-0.0059	-0.0022	1.0136	0.5303	0.0009	0.4633
$M(O_3)·(O_3)$	0.0236	-0.0148	0.9954	0.5199	0.0297	0.4462

3.2 Catalytic Cycles

For each of these catalysts, transition states were computed to study reaction barriers and determine preferred catalytic cycles. Figure 10 shows the Zr_NCCNO master cycle along with the computed energy change (kcal/mol) for each step. Here, we use the term master cycle to refer to a catalytic cycle comprised of two or more junior cycles. There are multiple junior cycles for producing propylene oxide from propene over this catalyst. The first junior cycles from 3 to 5 (non-ligand) oxygen atoms attached to the metal:

1. The bisperoxo complex reacts with propene to form the oxo peroxo complex plus propylene oxide.
2. The oxo peroxo complex reacts and one oxygen molecule to form the peroxo η^2-ozone complex.
3. The peroxo η^2-ozone complex transforms into the peroxo η^3-ozone complex.
4. The peroxo η^3-ozone complex reacts with propene to form propylene oxide and regenerate the bisperoxo complex.

Another junior cycles from 2 to 4 (non-ligand) oxygen atoms and passes through singlet states:

1. The dioxo complex and one oxygen molecule react to form the oxo η^2-ozone complex.
2. The oxo η^2-ozone complex transforms into the oxo η^3-ozone complex.
3. The oxo η^3-ozone complex reacts with propene to form the oxo peroxo complex plus propylene oxide.
4. The oxo peroxo complex reacts with propene to form propylene oxide and regenerate the dioxo complex.

A variation on this cycle passes through several triplet states to substantially lower the overall energy barrier. The singlet M'O(O_2) transforms into triplet M'O•(O_2) followed by propene addition to produce propylene oxide plus M'$(O)_{2,tri}$, which transforms into the singlet M'$(O)_2$. Alternatively, triplet M'O•(O_2) can be generated from triplet M'O via an exothermic reaction passing through M'O*(O_2). There is no transition barrier from triplet M'O to M'O*(O_2).

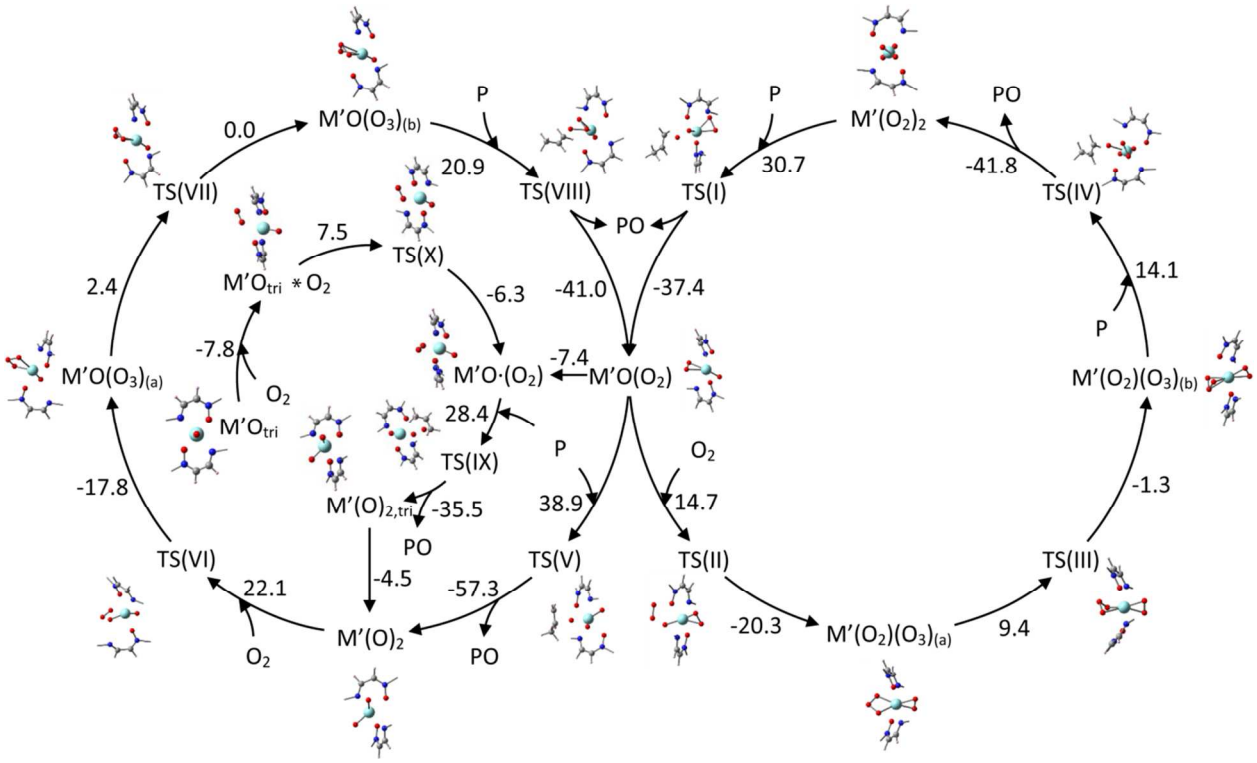

Figure 10: Master catalytic cycle for the NCCNO ligand architecture. SCF energies are in kcal/mol as computed by the B3LYP/LANL2DZ method. (For visual clarity, the molecular images display only part of the catalyst geometry.)

Transition states for forming propylene oxide are shown in Figure 11. In all of these transition states, the C=C bond of the approaching propene was oriented spiro to the departing O-O bond. Other propene approach paths were explored (e.g., Fig. S94), but these resulted in higher energy transition states. Our calculations revealed the preferred propene approach paths for peroxo and ozone groups are analogous. Moreover, the peroxo η^3-ozone complex has two spiro propene approach paths. As shown in Figure 11, one of these leads to forming the spiro bisperoxo complex and the other leads to forming the planar bisperoxo complex. The transition state for forming the planar bisperoxo complex is 3.7 kcal/mol higher in energy than the one for forming the spiro bisperoxo complex.

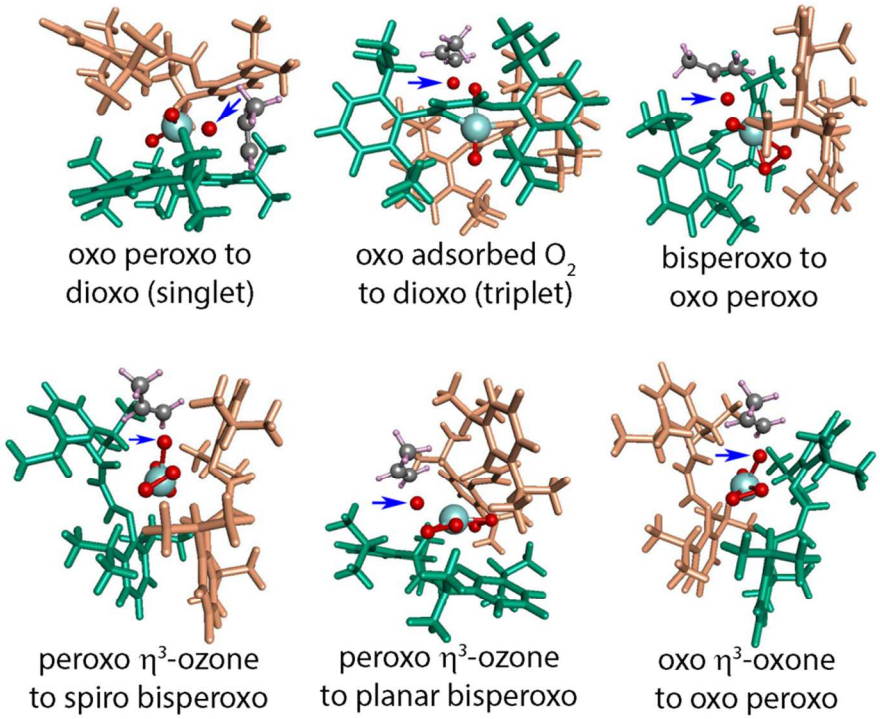

Figure 11: Transition states for forming propylene oxide over the Zr_NCCNO catalyst. Blue arrow points to the oxygen atom transferred to propene. Ligands colored orange and green. Other atoms: C (gray), H (small pink), O (red), Zr (cyan).

Figure 12 shows the Zr_ONCCNO master catalytic cycle along with the computed energy change (kcal/mol) for each step. This master cycle contains multiple junior cycles analogous to those described above for the Zr_NCCNO catalyst. Comparing Figure 10 and Figure 12, the transition state barriers for forming propylene oxide are slightly lower for the Zr_ONCCNO catalyst than for the Zr_NCCNO catalyst. A complete reaction pathway from butterfly bisperoxo complex to dioxo complex was also computed. The butterfly bisperoxo complex reacts with propene to generate the butterfly oxo peroxo complex plus propylene oxide, with an SCF energy barrier of 25.9 kcal/mol and a net reaction energy of -16.7 kcal/mol. The butterfly oxo peroxo complex reacts with propene to generate the dioxo complex plus propylene oxide, with an SCF energy barrier of 29.6 kcal/mol and an SCF net reaction energy of -6.2 kcal/mol. By these two steps, the butterfly bisperoxo complex will eventually go back into the main catalytic cycle. Although the butterfly bisperoxo complex is lower in energy than the spiro bisperoxo complex, we suspect the spiro bisperoxo complex will play a more dominant role in the reaction kinetics. The ONCCNO ligands are situated on opposite sides of the catalyst in the majority of catalyst forms (including the spiro bisperoxo complex). In contrast, the ligands are situated on the same side in the butterfly complexes. We believe forming the butterfly complexes may be a relatively slow process, due to challenges with migrating the ligand from one side of the catalyst to the other. In such case, the main catalytic cycle would proceed through the spiro bisperoxo complexes, as shown in Figure 12. However, if we are wrong in this belief, there is little consequence, because the energy barriers for forming propylene oxide over the spiro and

butterfly complexes are similar. The octahedral dioxo complex holds more potential to be a hindrance to the reaction kinetics. The SCF energy for transforming $M(O)_2$ into $M(O)_{2,oct}$ is -22.2 kcal/mol. Because the octahedral dioxo complex has low energy over the entire range of O atom chemical potential (Figure 7), it could act like a temporary dormant form. As explained in Section 3.3, this could raise the effective activation energy of the catalytic cycle from ~30 kcal/mol to ~58 kcal/mol.

Figure 13 shows the Zr_NCCN catalytic cycle along with the computed energy change (kcal/mol) for each step. Because the peroxo η^3-ozone complex does not exist for this catalyst, there is only one cycle. Unfortunately, this cycle has large energy barriers. To initiate the cycle, the spiro bisperoxo complex reacts with propene to form the oxo peroxo complex plus propylene oxide. For this step, the SCF energy barrier of 54.3 kcal/mol is large. Because the net reaction is computed to be endothermic and endergonic, there will be appreciable reversion from oxo peroxo complex plus propylene oxide back to bisperoxo complex plus propylene. The oxo peroxo complex reacts with propene to form the dioxo complex plus propylene oxide. The dioxo complex reacts with O_2 to form the oxo η^2-ozone complex which rearranges to form the oxo η^3-ozone complex. The oxo η^3-ozone complex reacts with propene to form propylene oxide and regenerate the oxo peroxo complex. The most concerning aspect of this cycle is the high energy barrier from the bisperoxo to the oxo peroxo complex. If the reaction is operated at very low O_2 pressures, where the O atom chemical potential is < -13 kcal/mol and the dioxo complex is the low energy form (Figure 8), the reversion back to bisperoxo complex might be avoided. Unfortunately, such conditions would make the dioxo to oxo η^2-ozone step energetically unfavorable. Consequently, this catalyst does not appear to be ideal for direct propene epoxidation.

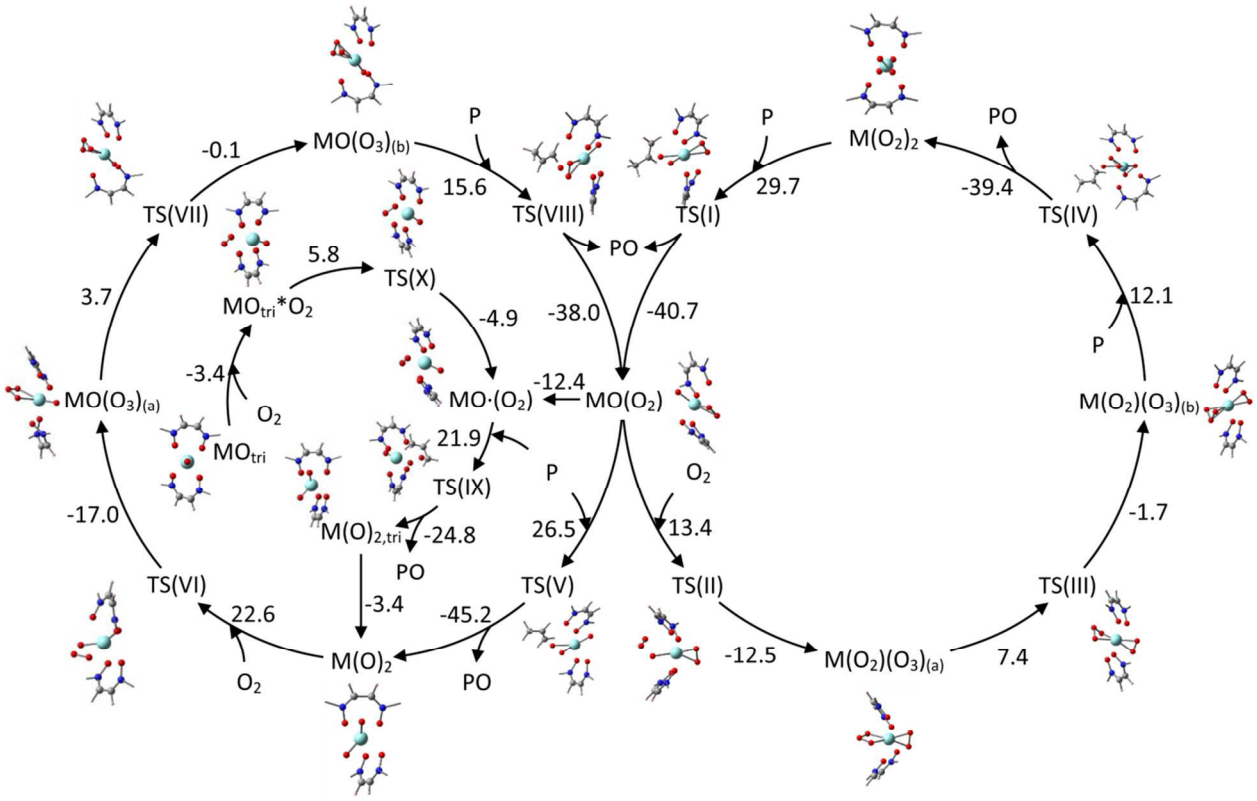

Figure 12: Master catalytic cycle for the ONCCNO ligand architecture. SCF energies are in kcal/mol as computed by the B3LYP/LANL2DZ method. (For visual clarity, the molecular images display only part of the catalyst geometry.)

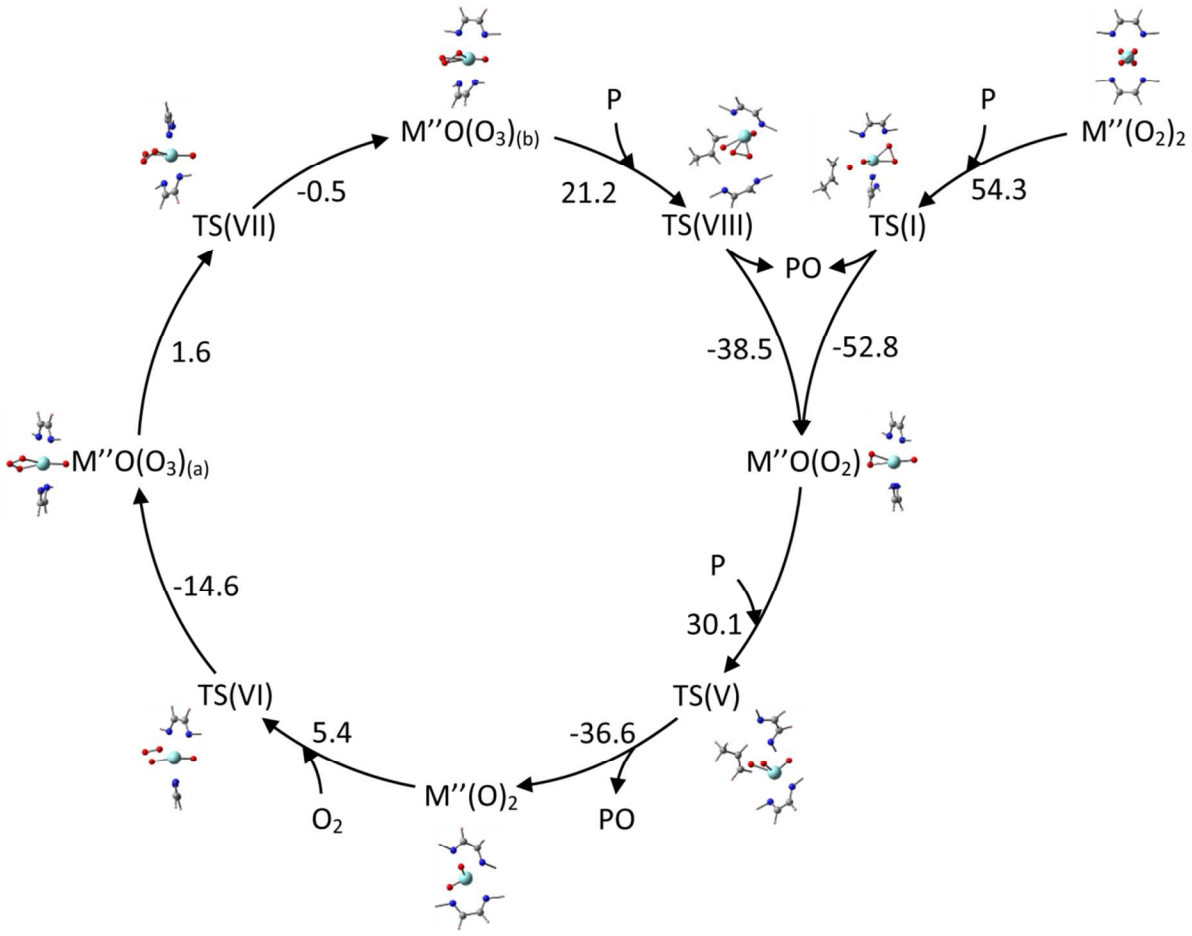

Figure 13: Catalytic cycle for the NCCN ligand architecture. SCF energies are in kcal/mol as computed by the B3LYP/LANL2DZ method. (For visual clarity, the molecular images display only part of the catalyst geometry.)

3.3 Energetic Spans

Energetic spans were also computed for each catalyst based on the SCF energy, E_{ZP}, enthalpy, and Gibbs free energy. As reviewed by Kozuch and Shaik,[54] the energetic span quantifies the apparent energy barrier for the entire catalytic cycle. The energetic span is the energy difference between the turn-over-frequency determining intermediate (TDI) and a subsequent turn-over-frequency determining transition state (TDTS).[54] The determination of TDI and TDTS is performed independently for the SCF energy, E_{ZP}, enthalpy, and Gibbs free energy. If we imagine the catalytic cycle as a wheel, we can choose any intermediate as the starting and ending point of the cycle. The TDI is that intermediate, which if chosen as a starting point, leads to the highest subsequent transition state energy (i.e., the TDTS) along the preferred catalytic cycle before returning.[54] The preferred catalytic cycle should be chosen to contain the catalyst resting state under reaction conditions. Chemical potential diagrams such as those presented in the Section 3.1 are useful for identifying the catalyst resting state under reaction conditions. The enthalpy energetic span provides an estimate of the apparent activation energy for the entire catalytic cycle.

Table 4: Computed reaction energies and energetic spans for the NCCNO ligand architecture

reactant	product	activation barrier				net rxn energy			
		E	E_{ZP}	H	G	E	E_{ZP}	H	G
M'$(O_2)_2$+P	M'O(O_2)+PO	30.7	30.8	30.9	42.7	-6.7	-5.7	-6.1	-5.6
M'O(O_2)+O_2	M'$(O_2)(O_3)_{(a)}$	14.7	16.3	15.4	26.7	-5.6	-3.3	-3.9	6.2
M'$(O_2)(O_3)_{(a)}$	M'$(O_2)(O_3)_{(b)}$	9.4	9.1	8.6	10.9	8.1	7.9	7.7	9.3
M'$(O_2)(O_3)_{(b)}$+P	M'$(O_2)_2$+PO	14.1	14.9	14.8	28.3	-27.7	-26.2	-26.6	-26.5
M'O(O_2)+P	M'$(O)_2$+PO	38.9	39.7	39.4	50.9	-18.4	-17.0	-17.4	-17.4
M'$(O)_2$+O_2	M'O$(O)_{3(a)}$	22.1	22.6	22.1	32.3	4.3	5.1	4.4	14.6
M'O$(O)_{3(a)}$	M'O$(O)_{3(b)}$	2.4	3.5	3.0	6.2	2.4	3.6	3.6	5.3
M'O$(O)_{3(b)}$+P	M'O(O_2)+PO	20.9	21.8	21.5	34.7	-20.2	-19.0	-19.5	-19
M'O_{tri}+O_2	M'O_{tri}*O_2	—	—	—	—	-7.8	-6.0	-6.4	6.4
M'O_{tri}*O_2	M'O·(O_2)	7.5	7.3	6.3	9.6	1.2	1.8	1.5	2.1
M'O·(O_2)+P	M'$(O)_{2,tri}$+PO	28.4	28.9	28.3	41.6	-7.2	-7.2	-7.3	-8.6
M'$(O)_{2,tri}$	M'$(O)_2$	—	—	—	—	-3.8	-2.4	-2.8	-0.4
M'O(O_2)	M'O·(O_2)	—	—	—	—	-7.4	-7.4	-7.3	-8.5
E_{span}		28.4	28.9	28.3	41.6				

As an example, we now compute the SCF energetic span for the Zr catalyst with NCCNO ligand architecture. The catalytic cycle in Figure 10 comprises multiple cycles due to the oxo η^3-ozone and peroxo η^3-ozone intermediates. The chemical potential diagram in Figure 6 shows singlet M'$(O_2)_{2(a)}$, triplet M'(O_2)•$(O_2)_{(a)}$, and triplet M'O are the low energy structures under reaction conditions. Singlet M'$(O_2)_{2(a)}$ and triplet M'(O_2)•$(O_2)_{(a)}$ have essentially identical energies and are preferred at higher oxygen chemical potential. Triplet M'O is preferred at lower oxygen chemical potential. Examining Figure 10, the peroxo η^3-ozone cycle contains the singlet

$M'(O_2)_{2(a)}$ intermediate and the triplet M'O intermediate connects up to the oxo η^3-ozone cycle. Therefore, these cycles appear to be reasonably chosen. For the oxo η^3-ozone cycle, the forward barrier is 28.4 kcal/mol and $M'O\bullet(O_2)$ is TDI and TS(IX) is TDTS. For the peroxo η^3-ozone cycle, the forward barrier is maximized at 30.7 kcal/mol if we choose $M'(O_2)_2$ as TDI and TS(I) as TDTS. Due to its lower barrier, we choose $M'O\bullet(O_2)$ as TDI and TS(IX) as TDTS with an SCF energetic span of 28.4 kcal/mol. However, the similar barriers suggest both the oxo η^3-ozone and peroxo η^3-ozone cycles may be kinetically important for this catalyst. Table 4 summarizes the thermodynamic data for each reaction step and the computed energetic spans for this catalyst. The enthalpy energetic span of 28.3 kcal/mol is our best estimate for the apparent activation energy for direct propene epoxidation over this catalyst.

Table 5: Computed reaction energies and energetic spans for the ONCCNO ligand architecture

reactant	product	activation barrier				net rxn energy			
		E	E_{ZP}	H	G	E	E_{ZP}	H	G
$M(O_2)_2$+P	$MO(O_2)$+PO	29.7	30.5	30.0	44.4	-11.0	-9.7	-10.2	-9.7
$MO(O_2)$+O_2	$M(O_2)(O_3)_{(a)}$	13.4	15.0	14.0	27.5	0.8	2.9	2.2	14.6
$M(O_2)(O_3)_{(a)}$	$M(O_2)(O_3)_{(b)}$	7.4	6.9	6.6	6.5	5.7	5.4	5.4	5.0
$M(O_2)(O_3)_{(b)}$+P	$M(O_2)_2$+PO	12.1	13.3	12.9	26.9	-27.4	-25.9	-26.3	-26.4
$MO(O_2)$+P	$M(O)_2$+PO	26.5	27.1	27.0	40.0	-18.7	-16.9	-17.4	-16.7
$M(O)_2$+O_2	$MO(O)_{3(a)}$	22.6	23.4	22.5	35.4	5.6	7.0	6.3	18.5
$MO(O)_{3(a)}$	$MO(O)_{3(b)}$	3.7	3.7	3.1	4.5	3.6	3.8	3.7	4.0
$MO(O)_{3(b)}$+P	$MO(O_2)$+PO	15.6	16.6	16.1	30.4	-22.3	-21.3	-21.6	-22.4
MO_{tri}+O_2	MO_{tri}*O_2	—	—	—	—	-3.4	-2.8	-2.4	6.1
MO_{tri}*O_2	$MO\cdot(O_2)$	5.8	6.8	5.7	11.0	0.9	2.9	1.8	7.3
$MO\cdot(O_2)$+P	$M(O)_{2,tri}$+PO	21.9	22.8	22.1	36.6	-3.0	-2.6	-2.8	-4.2
$M(O)_{2,tri}$	$M(O)_2$	—	—	—	—	-3.4	-1.2	-1.9	2.4
$MO(O_2)$	$MO\cdot(O_2)$	—	—	—	—	-12.4	-13.1	-12.7	-14.9
E_{span}		55.8	59.3	57.9	89.2				

We now consider energetic spans for the ONCCNO ligand architecture. The catalytic cycle in Figure 12 comprises multiple cycles due to the oxo η^3-ozone and peroxo η^3-ozone intermediates. The chemical potential diagram in Figure 7 shows $M'(O)_{2,oct}$ is the low energy form over the entire oxygen chemical potential range. However, the role of $M'(O)_{2,oct}$ in the catalytic process is as a reversible dormant state that does not contribute to the forward motion of the cycle. Therefore, we computed the energetic spans for this catalyst with and without including this octahedral complex. When the octahedral complex is neglected, the low energy catalyst forms are triplet MO at lower oxygen chemical potential and $MO\bullet(O_2)_{(a)}$ at higher oxygen chemical potential. Examining Figure 12, triplet MO and $MO\bullet(O_2)_{(a)}$ connect up to the oxo η^3-ozone cycle and its forward barrier is maximized at 24.8 kcal/mol if we choose singlet $M'(O_2)$ as TDI and TS(VIII) as TDTS. The SCF barrier for the peroxo η^3-ozone cycle is slightly higher at 29.7 kcal/mol with $M(O_2)_{2(a)}$ as TDI and TS(I) as TDTS. The octahedral complex can be included by assuming equilibrium between triplet $M(O)_{2,oct}$ and singlet $M(O)_2$. In this case,

triplet $M(O)_{2,oct}$ becomes the TDI and TS(VIII) becomes the TDTS. Adding the equilibration energy of 31.0 kcal/mol to form singlet $M(O)_2$ from triplet $M(O)_{2,oct}$ to the sequence of steps to form TS(VIII) from $M(O)_2$ gives a SCF energetic span of 31.0+22.6-17.0+3.7-0.1+15.6 = 55.8 kcal/mol for this catalyst. Table 5 summarizes the thermodynamic data for each reaction step and the computed energetic spans (including octahedral complex). The enthalpy energetic span of 57.9 kcal/mol is our best estimate for the apparent activation energy for direct propene epoxidation over this catalyst.

We now consider energetic spans for the NCCN ligand architecture. The catalytic cycle in Figure 13 comprise a single cycle due to the oxo η^3-ozone intermediate. Figure 8 shows $M''(O_2)_{2(a)}$ is the low energy form over the majority of the oxygen chemical potential range. The role of $M''(O_2)_{2(a)}$ in the catalytic process is as the catalyst resting state. Epoxidation occurs first by a reaction of propene with $M''(O_2)_{2(a)}$ to produce $M''O(O_2)$ plus propylene oxide. Further epoxidations can occur by a cycle from $M''O(O_2)$ to $M''(O)_2$ to $M''O(O)_{3(a)}$ to $M''O(O)_{3(b)}$ and regeneration of $M''O(O_2)$. The forward barrier for this oxo η^3-ozone cycle is maximized at 30.1 kcal/mol if we choose $M''O(O_2)$ as TDI and TS(V) as TDTS. However, the tendency of the catalyst to convert back to its resting state of $M''(O_2)_{2(a)}$ means the costly barrier of 54.3 kcal/mol to form TS(1) on the path to generate $M''O(O_2)$ will have to be repeated. Since multiple reaction paths (not shown) from various initial catalyst forms lead to the catalyst resting state, we cannot assume catalyst will revert to $M''(O_2)_{2(a)}$ solely by reaction of propylene oxide with $M''O(O_2)$ to generate $M''(O_2)_{2(a)}$ plus propene. Moreover, we cannot assume the reaction $M''(O_2)_2$+P ↔ $M''O(O_2)$+PO is at equilibrium, because propene is not at equilibrium with propylene oxide in the reactor. If we assume the catalyst readily converts back to its resting state by a variety of processes, this makes $M''(O_2)_{2(a)}$ the TDI and TS(I) the TDTS with an SCF energetic span of 54.3 kcal/mol. Table 6 summarizes the thermodynamic data for each reaction step and the computed energetic spans (using the assumption of rapid conversion back to the $M''(O_2)_{2(a)}$ resting state). If conversion back to $M''(O_2)_{2(a)}$ is somewhat hindered, the effective activation energy of the catalytic cycle will be lower than 54 but higher than 30 kcal/mol.

Table 6: Computed reaction energies and energetic spans for the NCCN ligand architecture

reactant	product	activation barrier				net rxn energy			
		E	E_{ZP}	H	G	E	E_{ZP}	H	G
$M''(O_2)_2$+P	$M''O(O_2)$+PO	54.3	53.7	54.1	63.9	1.5	2.4	2.1	1.8
$M''O(O_2)$+P	$M''(O)_2$+PO	30.1	28.6	29.5	34.5	-6.5	-6.1	-6.3	-8.7
$M''(O)_2+O_2$	$M''O(O)_{3(a)}$	5.4	6.5	5.8	18.5	-9.2	-6.8	-8.1	6.6
$M''O(O)_{3(a)}$	$M''O(O)_{3(b)}$	1.6	1.6	1.6	1.1	1.1	1.3	1.8	-0.5
$M''O(O)_{3(b)}$+P	$M''O(O_2)$+PO	21.2	19.5	20.4	25.9	-17.3	-15.7	-16.4	-13.9
E_{span}		54.3	53.7	54.1	63.9				

For comparison, we now mention several studies that reported DFT calculated energetic spans for propene epoxidation. Lei et al. reported an energetic span of ~42 kcal/mol for direct propene epoxidation over subnanometer silver clusters.[55] Joshi et al. reported an energetic span of 37.1 kcal/mol for propene epoxidation for the catalytic cycle $P + H_2 + O_2 \rightarrow PO + H_2O$ over

Au/TS-1 catalysts.[56] Lundin et al. reported an energetic span of 53.5 kcal/mol for the catalytic cycle P + H_2O_2 → PO + H_2O over a binuclear Ti dihydroxide model site.[57] de Visser et al. reported an energetic span of 31.2 kcal/mol for the catalytic cycle P + H_2O_2 → PO + H_2O in fluorinated alcohol solutions under mild conditions with no additional catalyst.[58]

We now consider the practical implications of the computed energetic spans. Rate constants for chemical reactions are commonly fit to the Arrhenius equation

$$k \approx A\exp\left(-E_a / k_B T\right) \qquad (1)$$

where A is the pre-exponential factor, E_a is the apparent activation energy, k_B is the Boltzmann constant, and T is the absolute temperature.[59] Despite its simplicity, the Arrhenius equation provides an excellent fit to a wide variety of kinetic experiments.[59] The pre-exponential factor A often increases as E_a increases along a related series of catalysts, but often not enough to cancel the dramatic drop in reactivity caused by increasing E_a.[60] Though not strictly identical in definition, the activation enthalpy $\Delta H^{\ddagger}$ (of which the computed enthalpy energetic span is an estimate) is expected to approximate the apparent activation energy, E_a, for the overall catalytic reaction. This is due to analogy between the Arrhenius equation involving E_a and the Eyring equation involving $\Delta H^{\ddagger}$, even though the pre-factor in the Eyring equation may explicitly depend on temperature.

These considerations allow us to make predictions about the rate constants for direct propene epoxidation by the Zr_NCCN, Zr_NCCNO, and Zr_ONCCNO systems. The difference in computed enthalpy energetic spans for the Zr_NCCN and Zr_NCCNO systems is ~25.8 kcal/mol. At 300 K, this corresponds to an exponential factor of exp(-28.5 kcal/mol/(R)(300K)) = 1.6×10^{-19}. However, because the pre-exponential factor often increases as E_a increases, we expect the direct propene epoxidation rate constant for Zr_NCCN to be ~10^{-12} times that for the Zr_NCCNO system. Even with a margin of error of a few orders of magnitude, our calculations predict the difference in epoxidation activity between the Zr_NCCN and Zr_NCCNO systems to be astronomical in magnitude. For all practical purposes, our calculations predict the epoxidation activity of the Zr_NCCN system to be nil. Similarly, the large computed enthalpy energetic span (57.9 kcal/mol) for the Zr_ONCCNO system (when the octahedral complex is included) suggests that formation of octahedral complexes in this system would lead to complete loss of epoxidation activity.

To understand this better, consider the relative temperatures that could be required to make the $\exp\left(-E_a / k_B T\right)$ factor similar for these catalysts. Specifically, the Zr_NCCN system may have to operate at a temperature of approximately 373 K × (54.1 kcal/mol) / (28.3 kcal/mol) ≈ 713 K (i.e., 440 °C) to achieve a reaction rate similar to that of the Zr_NCCNO system at 100 °C. However, it is extremely unlikely that the Zr_NCCN catalyst would be stable at temperatures near 440 °C, especially in the presence of reactive molecules such as O_2 and propene.

3.4 Catalyst Interconversion and Potential Side Reactions

The NCCN, NCCNO, and ONCCNO ligands can potentially interconvert by reacting the N atom of the ligand with an O atom. Table 7 summarizes the ligand interconversion energies for the spiro bisperoxo complexes. The M"$(O_2)_2$ complex is ~30 kcal/mol higher in energy than the $M(O_2)_2$ complex, and the M'$(O_2)_2$ is ~10 kcal/mol higher in energy than the $M(O_2)_2$ complex. However, the calculated free energies are closer. The M'$(O_2)_2$ complex is only 0.5 kcal/mol higher in free energy than the $M(O_2)_2$ complex, and the M"$(O_2)_2$ complex is only 8 kcal/mol higher in free energy than the $M(O_2)_2$ complex. Ligand interconversion appears to be a slow process under normal conditions. For example, Stanciu et al. reported the crystal structure of M"$(O_2)_2$ but did not mention any ligand interconversion even though the complex was observed for several days.[46]

Table 7: Energies (kcal/mol) of different ligation relative to the ONCCNO spiro bisperoxo complex

complex	abbrev.	E	E_{ZP}	H	G
NCCN spiro bisperoxo	M"$(O_2)_2$	30.8	25.5	26.6	8.0
NCCNO spiro bisperoxo	M'$(O_2)_2$	12.5	9.6	10.2	0.5
ONCCNO spiro bisperoxo	$M(O_2)_2$	0	0	0	0

An O atom can also potentially attack the ligand C=C group. At first we looked for epoxidation of the ligand C=C group. For the NCCN and NCCNO ligand architectures, DFT calculations started from epoxide-like geometries converged instead to ether-like geometries in which the O atom inserted between the ligand C atoms. These structures are shown in Figure 14. We refer to these as catalyst deformation products, rather than deactivation products, because there is no evidence yet to indicate whether these NCOCN and NCOCNO ligand architectures have higher or lower activity for direct propene epoxidation than the NCCN and NCCNO ligand architectures. For the ONCCNO ligand architecture, a different kind of deformation reaction was observed in which the ligand was split into two pieces by the O atom, as shown in Figure 14. The energies for each of these deformation products relative to the spiro bisperoxo complexes are given in Table 8. The computed energies show these deformation products have lower energies than the spiro bisperoxo complexes. We expect the activation barriers for forming the NCOCN and NCOCNO linkages and for splitting the ONCCNO ligand apart will be high, because they split C-C or C-N bonds.

Octahedral complexes play a key role for the ONCCNO system. The singlet ONCCNO octahedral dioxo complex discussed in Sections 3.1 to 3.3 is illustrated in Figure 14. The triplet has a similar structure, except the octahedral-like coordination of O atoms is less symmetrical in the triplet state because one of the O atoms attacks the ligand to form a C-O bond with length 1.37 Å (Fig. S135). Two additional kinds of triplet octahedral complexes were found for the ONCCNO system: (i) an octahedral complex containing adsorbed propylene oxide and (ii) an octahedral complex with transferred allylic H. The octahedral complex with transferred allylic H has transferred one of the allylic H atoms to form a Zr-OH group and the alpha C bonds to form a Zr-O-C linkage. We expect the barriers for forming octahedral complexes might be low, because they do not require C-C or C-N bond splitting. Transition state barriers for producing the

octahedral complex with transferred allylic H from the adsorbed PO octahedral complex are shown in parentheses. The low barriers (~5 kcal/mol) indicate this reaction should be facile.

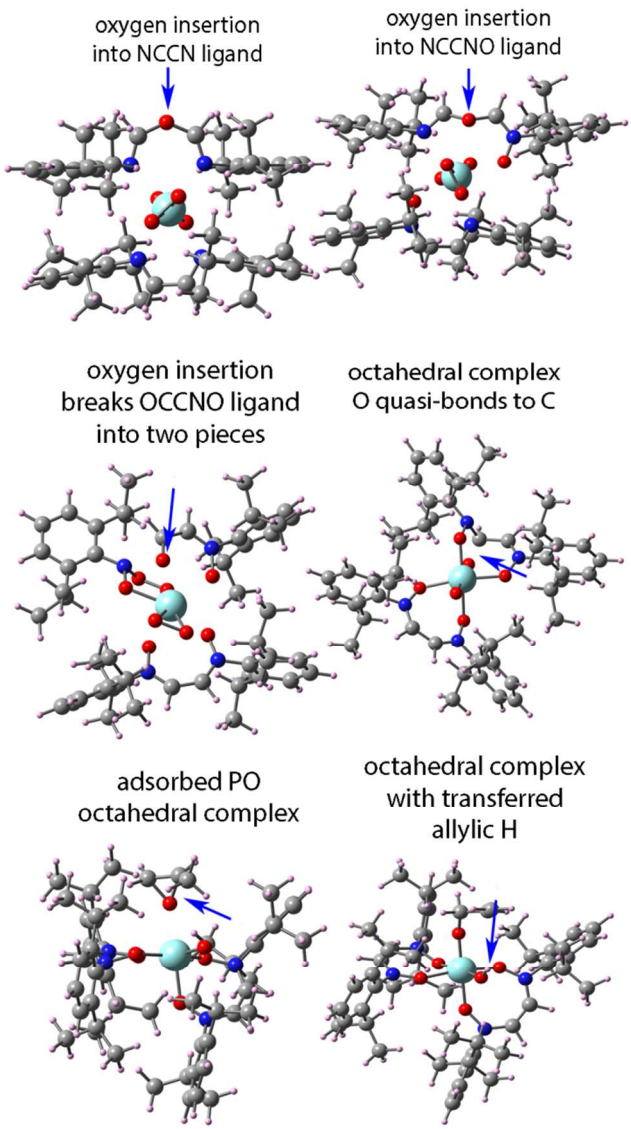

Figure 14: Potential catalyst deformation products

Table 8: Energies (kcal/mol) relative to the singlet spiro bisperoxo complexes[a]

catalyst system	deformation product	abbrev.	E	E_{ZP}	H	G
NCCN	O insertion into ligand	NCOCN	-25.0	-22.8	-23.4	-16.9
NCCNO	O insertion into ligand	NCOCNO	-16.7	-16.1	-16.1	-11.7
ONCCNO	O inserts to break ligand in half	ON+OCCNO	-15.2	-14.2	-15.0	-6.1
ONCCNO	singlet octahedral complex	$M(O)_{2,oct}$	-20.1	-21.5	-21.3	-32.9
ONCCNO	triplet octahedral complex	$M(O)_{2,oct}$	-28.9	-31.2	-30.5	-46.2
ONCCNO	adsorbed PO oct. complex		-7.6	-10.2	-8.8	-14.5
ONCCNO	octahedral complex with		-49.0	-55.3	-53.1	-60.1

transferred allylic H [b]	(7.6)	(5.1)	(4.6)	(4.3)

[a] The O atom chemical potential was taken to be that of molecular O_2. [b] The activation barrier to form this deactivation product is shown in parenthesis.

Ligand cyclization routes producing a metal-containing heterocyclic ring via reaction of a metal-adsorbed O_x group with a ligand C atom were also computed. Figs. S63, S103, and S64 show the reactant, transition state, and product for NCCNO ligand cyclization. Figs. S123, S165, and S124 show the reactant, transition state, and product for NCCNO ligand cyclization. However, all of these ligand cyclization reactions have little practical significance due to the relatively high energy of their products compared to other catalyst forms.

Finally, we wish to remark on the strength of propylene oxide and propylene adsorption. Fig. S77 shows the triplet M'O complex with adsorbed propylene oxide; the SCF propylene oxide adsorption energy of -4.6 kcal/mol indicates weak adsorption in this form. Figs. S65 and S66 shows the singlet M'O(O_2) complex with adsorbed propylene oxide; the SCF propylene oxide adsorption energy of -1.4 kcal/mol (relative to M'O(O_2)(a)) indicates weak adsorption in this form. Fig. S70 shows the singlet planar bisperoxo NCCNO complex with adsorbed propylene oxide; the SCF propylene oxide adsorption energy of -9.8 kcal/mol (relative to the planar bisperoxo complex) indicates moderate adsorption in this form. Fig. S138 shows the triplet M'O complex with adsorbed propylene oxide; the SCF propylene oxide adsorption energy of -2.6 kcal/mol indicates weak adsorption in this form. Finally, Fig. S78 shows a reacted propylene molecule with its terminal C atom bound to one of the O atoms of the NCCNO triplet dioxo structure; the SCF propylene adsorption energy of 16.1 kcal/mol (relative to the triplet dioxo complex) indicates unfavorable adsorption.

3.5 Structural Analysis

Finally, we make a few remarks about unusual structural aspects of the above complexes. We distinguished η^3-ozone from η^2-ozone complexation using the dihedral angle between the O_3 plane and the O-metal-O plane, where the two outside atoms of O_3 are used to determine the O-metal-O plane. Since these planes are parallel when the dihedral angle is 180° and perpendicular when the dihedral angle is 90°, we define η^2-ozone complexation as a dihedral angle > 135° and η^3-ozone complexation as a dihedral angle < 135°. Table 9 lists the dihedral angles for the singlet η^3-ozone complexes.

Table 9: Dihedral angle between the O_3 and O-Zr-O plane for singlet η^3-ozone complexes.

ligand architecture	complex	dihedral angle (°)
NCCN	oxo η^3-ozone	130.5
NCCNO	oxo η^3-ozone	121.7
NCCNO	peroxo η^3-ozone	106.2
ONCCNO	oxo η^3-ozone	114.0
ONCCNO	peroxo η^3-ozone	105.4

Using substructure searching, we searched the Cambridge Structural Database[61] for related crystal structures. A search for all Zr peroxo complexes returned two structures: BARMAK (bridged peroxo between two Zr) and NISDUP (Stanciu et al.[46]). A search for all Zr ozone complexes returned no matches. A search for all metal-ozone complexes returned four structures: FOYMIQ (Cs η^2-ozone complex), FOYMOW (K η^2-ozone complex), JEWVEM (Rb η^2-ozone complex), and JEWVEM01 (Rb η^2-ozone complex). Substructure searches for Ar-N(O)-C-C-N-Ar and Ar-N(O)-C-C-N(O)-Ar linkages returned only structures in which the C, N, or O atoms were bound to additional atoms in a manner that dramatically altered the connectivity.

We also performed similar substructure searches using Scifinder Scholar. A search for Zr peroxo structures returned ~200 substances. A search for all Zr ozone complexes returned no matches. Two Hf η^2-ozone complexes and three Ti η^2-ozone complexes were found. A search for all organometallic (i.e., structures containing organic ligands bound to a metal atom) η^3-ozone complexes returned only two studies describing organometallic complexes having a dihedral angle between the O_3 and O-metal-O planes less than 135°.[62, 63] The first was an experimental study of a Mn organometallic complex having a corresponding dihedral angle of 116°.[62] The second was a computational study of small metal complexes (e.g., $O_3Fe(CO)_3$ and $O_3Ru(CO)_3$).[63] Substructure searches for Ar-N(O)-C-C-N-Ar and Ar-N(O)-C-C-N(O)-Ar linkages returned only structures in which the C, N, or O atoms were bound to additional atoms in a manner that dramatically altered the connectivity. In summary, no Zr ozone complexes have been previously reported and the Ar-N(O)-CH-CH-N-Ar and Ar-N(O)-CH-CH-N(O)-Ar ligand frameworks are completely new.

Two papers by Lubben and Wolczanski described experiments in which O_2 inserted to form a Zr alkoperoxo intermediate (i.e., a $\boxed{Zr}-O(\mathrm{Me})-O$ group) that epoxidated a Zr-O-CMe_2-CH=CH_2 or Zr-O-CH_2-CH=CH_2 group in a stoichiometric reaction.[64, 65] The epoxidated group remained bound to the metal and only one of the O_2 atoms was transferred to form epoxide with the other being wasted to form a Zr-OMe group.[64, 65]

One of the anonymous reviewers pointed out the following statement made at the end of the 2007 article by Abu-Omar and co-workers: "Further spectroscopic, reactivity, and kinetic studies aimed at better understanding the formation of Zr^{IV} bis(peroxide) are in progress in our laboratory."[46] The reviewer remarked this statement suggests the Zr_NCCN system may have been tested for selective oxidation activity, but since no results to this effect have been published since the appearance of the 2007 article, the results of such experiments (if any) were likely negative. We subsequently wrote Drs. Mahdi Abu-Omar and Cornel Stanciu for clarification. They replied that experimental tests were performed, but no selective oxidation activity for the Zr_NCCN system was found. Specifically, it did not give epoxides or other products from olefins; it did not give sulfoxides from sulfides; and it did not react with methane or hexane.

As explained in Section 3.3 above, our computed energetic spans are consistent with nil epoxidation activity for the Zr_NCCN system at temperatures below ~200 °C and at higher temperatures the complex is likely to rapidly decompose. For comparison, the Zr_NCCNO

system is predicted to give an equivalent exp(-E_a/(RT)) factor at a temperature of (473 K)*(28.3 kcal/mol) / (54.1 kcal/mol) = 247 K (i.e., -26 °C).

We performed structural analysis to better understand the large difference in energetic spans between Zr_NCCN and Zr_NCCNO. Since the bisperoxo to oxo peroxo step is rate-determining in the Zr_NCCN system, the bond lengths, NOAP effective bond orders (EBOs),[49] and energetic parameters for this step are compared in Table 10. For clarity, we denote a ligand N atom not bound to a ligand O atom by the symbol N^t (i.e., terminal N). Examining Table 10, the Zr-O (ligand) EBOs are larger and distances smaller than those of Zr-N^t. Moreover, the NCCNO ligand bonds more effectively than the NCCN ligand to the metal center in both the reactant and TS: the sum of Zr-N^t/O EBOs in the reactant are 1.32 (NCCNO) and 0.84 (NCCN) and in the TS are 0.98 (NCCNO) and 0.70 (NCCN). Finally, the activation barrier is dramatically smaller for the NCCNO ligand compared to the NCCN ligand.

This can be rationalized as follows. The term 'bi-dentate' means 'two-toothed'. The NCCNO linkage has a longer 'tooth' on the O side which allows it to bite down more intensely on the metal—as evidenced by the larger Zr-O (ligand) EBOs and smaller Zr-O (ligand) distances compared to the Zr-N^t EBOs and distances. (However, using ONCCNO presents a new problem: the bite becomes too strong leading to the formation of inert octahedral complexes.) The bulky isopropyl substituents on the ligand's aromatic rings cause high steric congestion near the metal which limits how closely the bulky aromatic groups can approach the metal center. If these bulky groups are replaced with a smaller group (e.g., H atom), then the ligand's aromatic rings should be able to move slightly closer to the metal center. In this case, the ligand should be able to effectively bite down on the metal with shorter 'teeth'. The evidence for this is dramatic: once the isopropyl groups are replaced by H atoms in the bis-diimine Zr complex, the SCF activation barrier for the reaction P + bisperoxo → oxo peroxo + PO plummets from 54.3 kcal/mol to 32.3 kcal/mol with an associated decrease in Zr-N distances and increase in Zr-N EBOs. Work is underway in our group to compute complete reaction cycles for this catalyst. We also recommend the study of methyl and ethyl ortho substituents.

Table 10: Bond lengths, EBOs, and energies for the spiro bisperoxo to oxo peroxo propene epoxidation reaction over three Zr organometallic complexes

	Zr-N^t		Zr-O (ligand)		E (kcal/ mol)	E_{ZP} (kcal/ mol)	H (kcal/ mol)	G (kcal/ mol)
	length (Å)	NAOP EBO	length (Å)	NAOP EBO				
Zr_NCCNO catalyst								
reactant	2.42, 2.44	0.28, 0.30	2.27, 2.32	0.35, 0.39	0.0	0.0	0.0	0.0
TS	2.48, 4.15	0.01, 0.26	2.28, 2.31	0.34, 0.37	30.7	30.8	30.9	42.7
product	2.44	0.27	2.27	0.38	-6.7	-5.7	-6.1	-5.6
Zr_NCCN catalyst								
reactant	2.47	0.21	—	—	0.0	0.0	0.0	0.0
TS	2.51, 2.56, 2.61, 3.94	0.04, 0.21, 0.22, 0.23	—	—	54.3	53.7	54.1	63.9

product	2.45–2.50	0.23–0.27	—	—	1.5	2.4	2.1	1.8
diimine catalyst with isopropyl groups replaced by H atoms								
reactant	2.43	0.29	—	—	0.0	0.0	0.0	0.0
TS	2.40, 2.40, 2.50, 2.68	0.22, 0.29, 0.32, 0.33	—	—	32.3	32.0	32.2	42.7

As just demonstrated, too much steric congestion (e.g., Zr_NCCN system) leads to high activation barriers. On the other hand, too little steric congestion may potentially open up the door to new problems such as dimerization or oligomerization of the active species. For example, a bridged bisperoxo species between two Zr metal centers has been reported.[66] This clearly underscores the need to carefully optimize the amount of steric congestion near the metal center. Organometallic complexes containing a single metal center with high steric congestion cannot readily dimerize, because the high steric congestion hinders two metal centers from getting close to each other. Replacing the bulky isopropyl substituents with smaller substituents like H atoms might potentially allow dimerization or oligomerization of the active species; nevertheless, even in such case one could potentially thwart the potential possibility for catalyst dimerization by tethering the organometallic complex to a support. Such tethering could also facilitate catalyst separation from the reactants, products, and solvents.

4. Proposed Electrochemical Cell Process for Assembling the Catalysts

As illustrated in Figure 15, the catalyst could be assembled using an electrochemical cell. The cathode compartment could contain the following: (i) a liquid solution containing Zr^{2+} or Zr^{4+} ions (or Hf^{2+} or Hf^{4+} ions to make analogous hafnium catalysts) with a suitable counteranion(s), (ii) the desired ligand (L) dissolved in the liquid solution, (iii) a suitable electrode, (iv) optionally small amounts of O_2 at a controlled gas phase pressure, and (v) optionally other dissolved salts to facilitate ion transport through the selective ion permeable membrane. Optionally, the cathode electrode could be coated with (vi) a membrane to facilitate direct contact of $Zr^{2+}/Zr^{4+}/Hf^{2+}/Hf^{4+}$ and prevent direct contact of $ZrL_2(O_2)_x$ or $HfL_2(O_2)_x$ with the electrode material. The anode compartment could contain (vii) a suitable reductant, (viii) an anode electrode, and (ix) optionally dissolved salts in a liquid solution to facilitate ion transport through the selective ion permeable membrane. Preferably, the cathode and anode compartments would be separated by (x) a selective ion permeable membrane to facilitate and control ion transport between the two compartments. The selective ion permeable membrane should allow either (a) anions to flow from the cathode compartment to the anode compartment or (b) cations to flow from the anode compartment to the cathode compartment. A controlled external voltage source (xi) could be applied between the cathode and anode to drive the electrochemical reaction. The electrons would be collected at the anode, flow through the controlled external voltage source, and flow into the cathode. In the anode compartment, a suitable reductant could be used to produce electrons plus the corresponding reduced species. At the cathode, $Zr^{2+}/Zr^{4+}/Hf^{2+}/Hf^{4+}$ ions should be reduced and react with ligand and dissolved O_2 to produce $ZrL_2(O_2)_x$ or $HfL_2(O_2)_x$. If desired, the cathode and/or anode compartments could be stirred to

facilitate mass transfer between the gas phase, liquid phase, corresponding electrode, and selective ion permeable membrane.

Although we regard this electrochemical cell process as the preferred method for assembling the catalyst, other variations are possible. Using a selective ion permeable membrane should provide control over the process, but it could be omitted. Also, the anodes could be made from an expendable (i.e., sacrificial) material. In this case, the anode itself would act as the reductant. Alternatively, one could eliminate the entire anode compartment, selective ion permeable membrane, and external voltage control and just use an expendable (i.e., sacrificial) material for a one-pot process. Such a one-pot process was used by Stanciu et al. in which Mg metal was oxidized to Mg^{2+} ions in order to reduce $ZrCl_4$ to make the Zr catalyst with NCCN ligand architecture.[46] However, such a one-pot process may not be feasible with the oxygenated ligands (i.e., NCCNO, ONCCNO) described here, because Mg metal atoms could steal the terminal O atoms from the ligands (e.g., Mg + N(Ar)-CH-CH-N(Ar)O → MgO + N(Ar)-CH-CH-N(Ar)). Using distinct anode and cathode compartments separated by a selective ion permeable membrane and connected via an external voltage source is preferable, because it allows the process to be more precisely controlled to prevent O loss from the ligands.

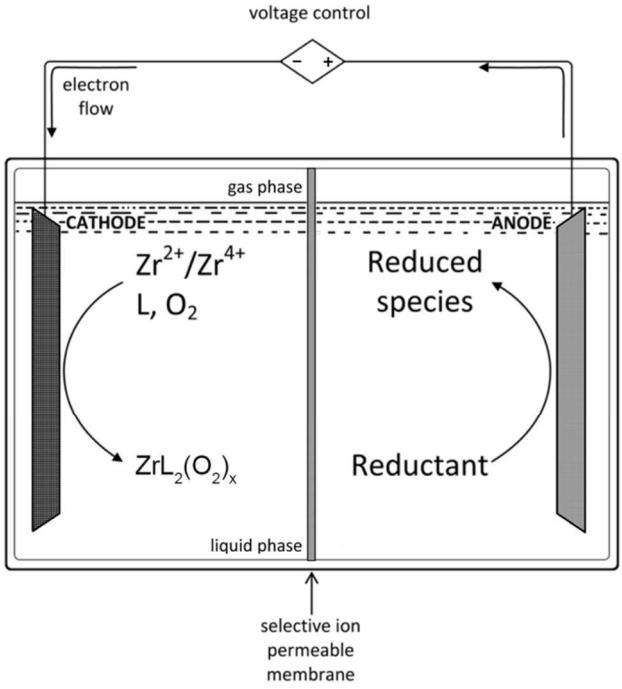

Figure 15: Proposed electrochemical cell process for assembling the catalysts

5. Proposed Chemical Process Flow Diagram for Direct Propene Epoxidation

General operating targets (e.g., temperature range, pressure range, composition range, catalyst separation method, etc.) should be considered when designing catalysts for a particular application. For homogeneous catalysts, one of the main factors that must be considered is how to separate the catalyst from the reaction products. The difficulty of separating reactants from

products is also a major consideration. If separating reactants from products is easy, the reactor can be operated at low conversion with reactant recycle. On the other hand, if separating reactants from products is difficult, the reactor should be designed to operate at high conversion. These factors directly influence the catalyst design, because they place constraints on the conversion which must be achieved by the catalyst. Safety factors are also a major consideration. Specifically, the vapor composition inside the reactor should be kept out of the explosive regime. This places constraints on the ranges of vapor compositions and pressures at which the catalyst must operate.

A chemical process flow diagram can be a useful tool for identifying general process characteristics that impact catalyst design. Figure 16 is a proposed preliminary chemical process flow diagram for directly oxidizing propene to propylene oxide using molecular oxygen (and/or dry air) as the oxidant. This process is designed to use a homogeneous or finely divided heterogeneous catalyst in continuous stirred tank reactors with vigorous agitation to facilitate rapid mass transfer between the liquid and vapor phases. The process is intended to operate at moderate temperatures and pressures with modest energy requirements.

We now summarize the main features of this process. For safety reasons, the vapor compositions, temperatures, and pressures should be carefully controlled throughout the process to prevent explosive conditions. For this reason, the process should use an inert gas diluent (such as N_2) which could be supplied by a purified N_2 source and (optionally) a dry air source. (The ratio of O_2 to N_2 in dry air is approximately 1:4.) O_2 could also be supplied via a purified O_2 source; however, if desired all of the O_2 could be supplied via a dry air source. The dry air, O_2, and/or N_2 streams should be mixed to form a diluted O_2 stream that should be subsequently mixed with propene (fresh and recycled). A pump should deliver this gas mixture to the first reactor.

Each reactor should be an agitated tank reactor with vigorous stirring and baffles to maximize vapor-liquid contact for efficient mass transfer. The reactors should use an aprotic solvent that is less volatile than propylene oxide. Aprotic solvents are recommended to avoid side reactions that may be caused by labile H^+ ions. Toluene (normal boiling point of approximately 111° C) is an example of an aprotic solvent that could be used. Each reactor should contain means to control the temperature such as heat exchange coils or jacketing. The number of reactors could vary from one to several. The reactors could be arranged in parallel, serial, or a combination of serial and parallel. Each reactor should be preceded by a pump and followed by one or more control valves to control the reactor pressure and flow rates into and out of the reactor. (Valves are not shown on the accompanying process flow diagram. Valves should be located throughout the process between all the major operating units to allow flow controls and safety shutoffs.) Gas mixers should control the input stream composition to each reactor. For safety reasons, the gas mixer to each reactor should be set to supply a flush of pure N_2 to the reactor when an emergency shut-down is required. Under normal operating conditions, the gas mixer to each reactor should supply some desired mixture of O_2, dry air, N_2, fresh propene, recycled propene, and/or intermediate process streams that have been mostly stripped of

propylene oxide and solvent. This should precisely control the vapor composition in each reactor to avoid explosive conditions.

Each reactor's exit stream may be drawn from the vapor phase to retain catalyst in the reactor. In this case, the exit stream from the reactor should pass through a condenser into a flash drum. The condenser and flash drum should liquify solvent and propylene oxide and allow less volatile components to remain in the vapor phase. Because the normal boiling point of propylene oxide is approximately 34° C, these condensers could operate near room temperature using cooling water or other suitable coolant. If desired, each reactor could be followed by its own condenser and flash drum or the exit streams from several reactors could be joined before entering a condenser and flash drum.

The vapor phase exit from the condenser (marked COND3) and flash drum (marked FLASH3) following the final reactor should be fed into another condenser (marked COND4) and flash drum (marked FLASH4) that operates at a low temperature and/or high pressure to liquify propene while leaving O_2 and N_2 in the vapor phase. COND4 should perform a combination of heat exchange and/or compressing to lower the temperature and/or raise the pressure until propene liquifies. (The normal boiling point of propene is -48° C.) This propene should be subsequently vaporized in a heat exchanger and recycled with a pump. The vapor exhaust from FLASH4 should consist mainly of N_2 and O_2 with trace amounts of other gases (e.g., propene, propylene oxide, solvent, and argon if dry air is used in the process) that could be sent to flare or otherwise vented, possibly after scrubbing to remove trace organic components or otherwise treated to meet emission standards.

The mixture of propylene oxide and solvent liquified in the first flash drum after each reactor (marked FLASH1, FLASH2, and FLASH3 in the example process flow diagram) should be joined into a common stream fed with a pump to a distillation unit. This distillation unit should separate solvent from propylene oxide. If any by-products are formed, they should also be separated from propylene oxide and solvent in this distillation unit or an auxiliary separation unit. The purified solvent should be recycled back to each reactor using a pump. The purified propylene oxide is the desired chemical product.

The catalyst and solvent in each reactor would need to be replenished due to (hopefully slow) catalyst deactivation and solvent losses. This replenishment could be performed by equipping each reactor with liquid purge and makeup streams. This replenishment could be performed intermittently (e.g., during equipment down times) or in a slow but continuous fashion during normal operation. Also, it may be desirable to feed trace amounts of fresh ligand (either intermittently or continuously) into the solvent recycle stream to replenish slow ligand losses.

The operational pressures and temperatures in the reactor units should be chosen to give appropriate catalyst activity. We expect the ideal reactor temperature to lie in the range of 50 to 150° C. This implies the catalyst should preferably be designed to have high activity, selectivity, and stability over this temperature range. If a reactor temperature above 100° C is used, a solvent less volatile than toluene would be best. We expect the reactors to operate at pressures between

0.1 and 100 bar. We expect the distillation unit to operate near a pressure of ~1 bar and a temperature range between ~30° C and the solvent's normal boiling point.

Key characteristics of this process are due to the large differences in normal boiling points of the reactants, desired product, and solvent. Because the normal boiling point of propylene oxide (34° C) is close to ambient conditions, propylene oxide could be removed from the reactor either via the vapor or liquid phase. The potential ability to remove propylene oxide from the reactor via the vapor phase and subsequently condense it under mild conditions using cooling water (~18 ° C) could facilitate product separation from the catalyst (which would remain in the reactor) and the reactants (which would not be condensed by the cooling water). This would help keep the separation energy requirements low and facilitate propene recycle. Because of the ability to recycle propene, the one-pass conversion does not need to approach 100%.

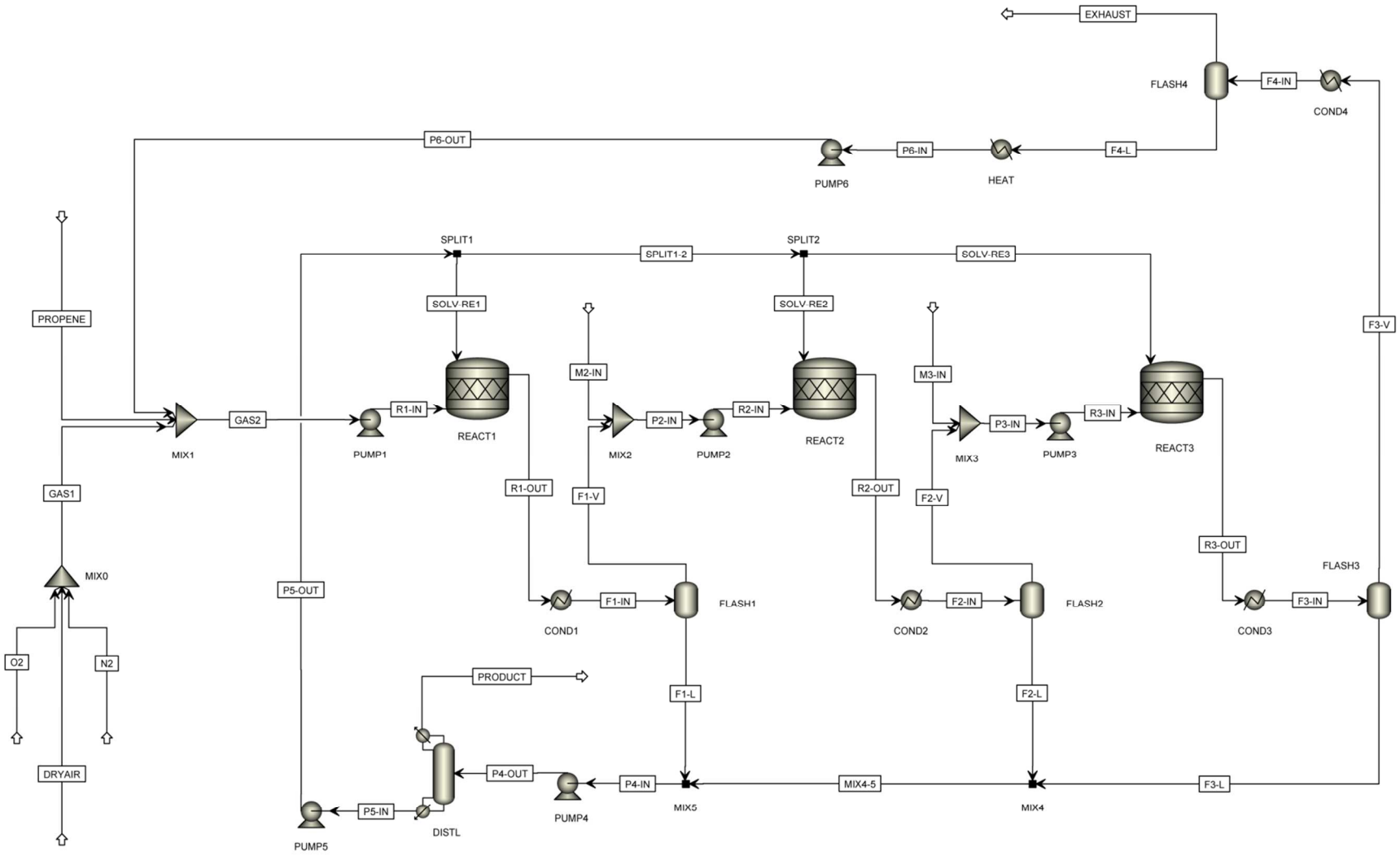

Figure 16: Proposed process flow diagram for the direct epoxidation of propene using molecular oxygen oxidant

6. Conclusions

In this article, we used DFT computations to design a new kind of catalytic route for direct propene epoxidation using molecular oxygen as the oxidant. By eliminating co-reactant, this process can potentially eliminate or reduce co-product/by-product formation. If successful, this would give large economic and environmental benefits. Formation of a η^3-ozone intermediate (e.g., oxo η^3-ozone and peroxo η^3-ozone complexes) is a crucial step in the catalytic cycle. Key steps in the catalytic cycle are: (a) the η^3-ozone group adds an O atom to substrate (e.g., propene) to form substrate oxide (e.g., propylene oxide) plus a peroxo or adsorbed O_2 group, (b) the peroxo or adsorbed O_2 group adds an O atom to substrate to form substrate oxide plus an oxo group, (c) an oxygen molecule adds to the oxo group to generate an η^2-ozone group, and (d) the η^2-ozone group rearranges to regenerate the η^3-ozone group.

Our computations introduced two new classes of Zr organometallic complexes that have dinitrone and imine-nitrone based bis-bidentate ligands, and we proposed an electrochemical cell process for assembling these catalysts. We used DFT calculations to compute chemical potential diagrams and complete catalytic cycles with transition states for three homogeneous catalysts: (a) Zr(N(Ar)-CH-CH-N(Ar))$_2$(O$_2$)$_2$, (b) Zr(N(Ar)-CH-CH-N(Ar)-O)$_2$(O$_2$)$_2$, and (c) Zr(O-N(Ar)-CH-CH-N(Ar)-O)$_2$(O$_2$)$_2$ with Ar = C_6H_3-2,6-^{i}Pr$_2$. To the best of our knowledge, the calculated enthalpy energetic span of ~28.3 kcal/mol for the Zr_NCCNO catalyst with imine-nitrone based ligation is lower than for any previously reported direct propene epoxidation catalyst. The Zr_ONCCNO catalyst with dinitrone-based ligation had a large computed enthalpy energetic span (~57.9 kcal/mol) due to the formation of low energy octahedral complexes that act as dormant resting states. Moreover, we showed the inertness of the Zr_NCCN system is mainly due to too high steric congestion, and the enthalpy barrier of the key reaction step can be lowered from 54.1 kcal/mol to 32.2 kcal/mol by replacing the bulky isopropyl groups on the aromatic rings with H atoms.

Based on our results, we recommend further computational and experimental studies focusing on selective oxidation reactions via organometallic η^3-ozone intermediates using molecular oxygen as the oxidant. Our results suggest that future studies of selective oxidation reactions over bis-bidendate diimine, imine-nitrone, and dinitrone based Group 4 organometallic catalysts should focus on systems with carefully optimized amounts of steric congestion. We recommend further computational screening to identify new catalysts with even lower energetic spans than the Zr_NCCNO system. For example, it would be desirable to further decrease the computed enthalpy energetic span for direct propene epoxidation to <20 kcal/mol. Similar to what we have done here, such screening should also include an evaluation of factors affecting catalyst stability and selectivity. Further progress also requires the synthesis and experimental testing of these or similar catalysts.

When designing new catalysts, it is useful to have at the outset a general idea of the types of processes in which the catalysts could be used. Accordingly, we proposed a process flow diagram for direct propene epoxidation that should be compatible with organometallic catalysts like the ones studied here. This process should operate at moderate temperatures and pressures

using continuous stirred tank reactors with vigorous agitation to facilitate rapid mass transport between gas and liquid phases. We recommend using an aprotic solvent to avoid side reactions caused by labile H^+ ions. Key features of this process are due to the large differences in boiling points between the catalyst, reactants, and products. Because the normal boiling point of propylene oxide is only slightly above room temperature, it could be removed from the reactors via the vapor phase. This would facilitate catalyst separation, because the catalyst would remain in the liquid phase as the products, reactants, and carrier gas are drawn off via the gas phase. Due to its moderate normal boiling point (34 °C), propylene oxide could be subsequently condensed in a heat exchanger by passing chilled water (or other suitable coolant) through cooling coils. The uncondensed vapor containing carrier gas, unreacted propene, and other volatiles should be subjected to another condenser operating at higher pressure and/or lower temperature to condense the propene, which would be recycled to the reactors.

The principles described in this article are fairly broad and can be applied to a variety of catalyst architectures and substrates. For example, we have computed chemical potential diagrams and complete catalytic cycles with transition states for direct propene epoxidation using the Hf analogs of the three Zr catalysts studied here. The Hf analogs gave similar results to the Zr systems and will be described in a forthcoming paper. Extensions to other transition metals (e.g., Ti) might also be possible. Because the role of substrate during the catalytic cycle is mainly to be a permanent receptor for oxygen atoms, it is clear the basic mechanism described here for selective oxidation of propene could also be used to selectively oxidize a wide variety of other substrates. This belief is supported by the observation that the chemical potential diagram (e.g., Figure 6, Figure 7, and Figure 8) describing the stability of different catalyst forms as a function of oxygen chemical potential is essentially independent of the substrate. Of course, many of the transition state energies are substrate dependent. Many ligand variations can also be envisioned such as: (a) various substituents (e.g., H, alkyl, halogen, alkoxy, etc.) in the *ortho*, *meta*, and *para* positions of the ligand's aromatic rings, (b) various substituents (e.g., H, alkyl, halogen, alkoxy, etc.) for g and g' groups in the N(Ar)-C(g)-C(g')-N(Ar), N(Ar)-C(g)-C(g')-N(Ar)-O and O-N(Ar)-C(g)-C(g')-N(Ar)-O linkages, (c) using naphthelenyl or other fuzed rings for the Ar groups, and (d) connecting the N atoms using an aromatic ring (e.g., N(Ar)-(C_6H_4)-N(Ar), N(Ar)-(C_6H_4)-N(Ar)-O, or O-N(Ar)-(C_6H_4)-N(Ar)-O). Since our DFT calculations revealed increased stability of the NCOCN and NCOCNO type ligand linkages, we think it would also be useful to explore these kinds of ligand variations. These ligand architectures should be carefully chosen to optimize catalyst activity, selectivity, and stability.

Acknowledgements: Supercomputing resources were provided by the Extreme Science and Engineering Discovery Environment (XSEDE). XSEDE is funded by NSF grant OCI-1053575. XSEDE project grant TG-CTS100027 provided allocations on the Steele supercomputing cluster at Purdue University and the Trestles supercomputing cluster at the San Diego Supercomputing Center (SDSC). The authors sincerely thank the staff of XSEDE, Information Technology at

Purdue (ITaP), and SDSC. The authors and NMSU's Office of Intellectual Property (Arrowhead Center, Inc.) have applied for a patent on some of the results described in this paper.

Electronic Supplementary Information: DFT-optimized geometries and energies; imaginary frequency for each transition state; singlet-triple crossing curves for O_2 addition to dioxo complexes; constrained geometry optimization curve showing the absence of a peroxo η^3-ozone intermediate for the Zr_NCCN catalyst.

7. References

1. E. M. Kirschner, *Chem. Eng. News*, 1995, **73**, 16-20.
2. D. Kahlich, U. Wiechern and J. Linder, in *Ullmann's Encyclopedia of Industrial Chemistry*, Wiley-VCH Verlag GmbH & Co. KGaA, 2012, vol. 30, pp. 313-335.
3. D. J. Suh, O. O. Park and K. H. Yoon, *Polymer*, 2000, **41**, 461-466.
4. B. Weyershausen, K. Hell and U. Hesse, *Green Chem.*, 2005, **7**, 283-287.
5. E. P. Johnson, *Environ. Impact Assess.*, 2012, **32**, 156-164.
6. L. C. Rowe, R. L. Chance and M. S. Walker, *Mater. Performance*, 1983, **22**, 17-23.
7. P. Harry, E. Jobard, M. Briand, A. Caubet and A. Turcant, *Pediatrics*, 1998, **102**, article number e31:31-33.
8. P. Leth and M. Gregersen, *Forensic Science International*, 2005, **155**, 179-184.
9. T. Zar, C. Graeber and M. A. Perazella, *Seminars in Dialysis*, 2007, **20**, 217-219.
10. R. A. Vansanten and H. Kuipers, *Advances in Catalysis*, 1987, **35**, 265-321.
11. K. Yokozaki, H. Ono and A. Ayame, *Appl. Catal. A*, 2008, **335**, 121-136.
12. T. A. Nijhuis, M. Makkee, J. A. Moulijn and B. M. Weckhuysen, *Ind. Eng. Chem. Res.*, 2006, **45**, 3447-3459.
13. G. Z. Lu and X. B. Zuo, *Catal. Lett.*, 1999, **58**, 67-70.
14. J. Q. Lu, M. F. Luo, H. Lei and C. Li, *Appl. Catal. A*, 2002, **237**, 11-19.
15. A. Pulido, P. Concepcion, M. Boronat and A. Corma, *J. Catal.*, 2012, **292**, 138-147.
16. S. Shin and D. Chadwick, *Ind. Eng. Chem. Res.*, 2010, **49**, 8125-8134.
17. G. Blanco-Brieva, M. C. Capel-Sanchez, M. P. de Frutos, A. Padilla-Polo, J. M. Campos-Martin and J. L. G. Fierro, *Ind. Eng. Chem. Res.*, 2008, **47**, 8011-8015.
18. H. Lee, T. Shi, D. Busch and B. Subramaniam, *Chem. Eng. Sci.*, 2007, **62**, 7282-7289.
19. M. Ghanta, D. Fahey, D. Busch and B. Subramaniam, *ACS Sustainable Chem. Eng.*, 2013, **1**, 268-277.
20. F. Cavani, *Catal. Today*, 2010, **157**, 8-15.
21. F. Cavani, *J..Chemical Technol. Biotechnol.*, 2010, **85**, 1175-1183.
22. M. Kahn, A. Seubsai, I. Onal and S. Senkan, *Top. Catal.*, 2010, **53**, 86-91.
23. N. Mimura, S. Tsubota, K. Murata, K. K. Bando, J. J. Bravo-Suarez, M. Haruta and S. T. Oyama, *Catal. Lett.*, 2006, **110**, 47-51.
24. Y. Y. Liu, K. Murata and M. Inaba, *Chem. Commun.*, 2004, 582-583.
25. A. C. Kizilkaya, M. F. Fellah and I. Onal, *Chem. Phys. Lett.*, 2010, **487**, 183-189.
26. W. Long, Q. Zhai, J. He, Q. Zhang, W. Deng and Y. Wang, *ChemPlusChem*, 2012, **77**, 27-30.
27. A. Pulido, P. Concepcion, M. Boronat and A. Corma, *J. Catal.*, 2012, **292**, 138-147.
28. J. Q. Lu, M. F. Luo, H. Lei, X. H. Bao and C. Li, *J. Catal.*, 2002, **211**, 552-555.

29. Y. Lei, F. Mehmood, S. Lee, J. Greeley, B. Lee, S. Seifert, R. E. Winans, J. W. Elam, R. J. Meyer, P. C. Redfern, D. Teschner, R. Schlogl, M. J. Pellin, L. A. Curtiss and S. Vajda, *Science*, 2010, **328**, 224-228.
30. J. H. Huang, T. Takei, H. Ohashi and M. Haruta, *Appl. Catal. A*, 2012, **435**, 115-122.
31. A. Seubsai, M. Kahn and S. Senkan, *ChemCatChem*, 2011, **3**, 174-179.
32. J. H. Huang and M. Haruta, *Res. Chem. Intermediat.*, 2012, **38**, 1-24.
33. E. M. McGarrigle and D. G. Gilheany, *Chem. Rev.*, 2005, **105**, 1563-1602.
34. G. Grigoropoulou, J. H. Clark and J. A. Elings, *Green Chem.*, 2003, **5**, 1-7.
35. Q. H. Xia, H. Q. Ge, C. P. Ye, Z. M. Liu and K. X. Su, *Chem. Rev.*, 2005, **105**, 1603-1662.
36. H. Adolfsson and D. Balan, in *Aziridines and Epoxides in Organic Synthesis*, ed. A. K. Yudin, Wiley-VCH, Weinheim, Germany, 2006, pp. 185-228.
37. K. Jorgensen, *Chem. Rev.*, 1989, **89**, 431-458.
38. B. Lane and K. Burgess, *Chem. Rev.*, 2003, **103**, 2457-2473.
39. D. Deubel, J. Sundermeyer and G. Frenking, *J. Am. Chem. Soc.*, 2000, **122**, 10101-10108.
40. D. Deubel, G. Frenking, P. Gisdakis, W. Herrmann, N. Rosch and J. Sundermeyer, *Acc. Chem. Res.*, 2004, **37**, 645-652.
41. P. Gisdakis, I. Yudanov and N. Rosch, *Inorg. Chem.*, 2001, **40**, 3755-3765.
42. M. Kuznetsov and J. Pessoa, *Dalton Trans.*, 2009, 5460-5468.
43. A. Comas-Vives, A. Lledos and R. Poli, *Chem. Eur. J.*, 2010, **16**, 2147-2158.
44. M. Herbert, F. Montilla, E. Alvarez and A. Galindo, *Dalton Trans.*, 2012, **41**, 6942-6956.
45. J. Groves and R. Quinn, *J. Am. Chem. Soc.*, 1985, **107**, 5790-5792.
46. C. Stanciu, M. E. Jones, P. E. Fanwick and M. M. Abu-Omar, *J. Am. Chem. Soc.*, 2007, **129**, 12400-12401.
47. T. A. Manz and D. S. Sholl, *J. Chem. Theory Comput.*, 2010, **6**, 2455-2468.
48. T. A. Manz and D. S. Sholl, *J. Chem. Theory Comput.*, 2012, **8**, 2844-2867.
49. T. A. Manz and D. S. Sholl, in *Computational Catalysis*, eds. A. Asthagiri and M. Janik, RSC Publishing, Cambridge, UK, 2014, pp. 192-222.
50. A. D. Becke, *J. Chem. Phys.*, 1993, **98**, 5648-5652.
51. P. J. Stephens, F. J. Devlin, C. F. Chabalowski and M. J. Frisch, *J. Phys. Chem.*, 1994, **98**, 11623-11627.
52. M. J. Frisch, G. W. Trucks, H. B. Schlegel, G. E. Scuseria, M. A. Robb, J. R. Cheeseman, G. Scalmani, V. Barone, B. Mennucci, G. A. Petersson, H. Nakatsuji, M. Caricato, X. Li, H. P. Hratchian, A. F. Izmaylov, J. Bloino, G. Zheng, J. L. Sonnenberg, M. Hada, M. Ehara, K. Toyota, R. Fukuda, J. Hasegawa, M. Ishida, T. Nakajima, Y. Honda, O. Kitao, H. Nakai, T. Vreven, J. A. J. Montgomery, J. E. Peralta, F. Ogliaro, M. Bearpark, J. J. Heyd, E. Brothers, K. N. Kudin, V. N. Staroverov, T. Keith, R. Kobayashi, J. Normand, K. Raghavachari, A. Rendell, J. C. Burant, S. S. Iyengar, J. Tomasi, M. Cossi, N. Rega, J. M. Millam, M. Klene, J. E. Knox, J. B. Cross, V. Bakken, C. Adamo, J. Jaramillo, R. Gomperts, R. E. Stratmann, O. Yazyev, A. J. Austin, R. Cammi, C. Pomelli, J. W. Ochterski, R. L. Martin, K. Morokuma, V. G. Zakrzewski, G. A. Voth, P. Salvador, J. J. Dannenberg, S. Dapprich, A. D. Daniels, O. Farkas, J. B. Foresman, J. V. Ortiz, J. Cioslowski and D. J. Fox, Gaussian, Inc., Wallingford CT, Gaussian 09, Revision C.01, 2010.
53. T. A. Manz and D. S. Sholl, *J. Chem. Theory Comput.*, 2011, **7**, 4146-4164.
54. S. Kozuch and S. Shaik, *Acc..Chem. Res.*, 2011, **44**, 101-110.

55. Y. Lei, F. Mehmood, S. Lee, J. Greeley, B. Lee, S. Seifert, R. E. Winans, J. W. Elam, R. J. Meyer, P. C. Redfern, D. Teschner, R. Schlogl, M. J. Pellin, L. A. Curtiss and S. Vajda, *Science*, 2010, **328**, 224-228.
56. A. Joshi, W. Delgass and K. Thomson, *J. Phys. Chem. C*, 2007, **111**, 7841-7844.
57. A. Lundin, I. Panas and E. Ahlberg, *J. Phys. Chem. A*, 2009, **113**, 282-290.
58. S. de Visser, J. Kaneti, R. Neumann and S. Shaik, *J. Org. Chem.*, 2003, **68**, 2903-2912.
59. K. Laidler, *J. Chem. Educ.*, 1984, **61**, 494-498.
60. R. Agrawal, *J. Therm. Anal.*, 1986, **31**, 73-86.
61. F. Allen*, Acta Crystallogr., Sect. B: Struct. Sci., 2002*, **58**, 380-388.
62. V. Gotte, J. Goulon, C. Goulon-Ginet, A. Rogalev, C. Natoli, K. Perie, J. Barbe and R. Guilard, *J. Phys. Chem. B*, 2000, **104**, 1927-1938.
63. B. Flemmig, P. Wolczanski and R. Hoffmann, *J. Am. Chem. Soc.*, 2005, **127**, 1278-1285.
64. T. Lubben and P. Wolczanski, *J. Am. Chem. Soc.*, 1985, **107**, 701-703.
65. T. Lubben and P. Wolczanski, *J. Am. Chem. Soc.*, 1987, **109**, 424-435.
66. G. C. Wang, H. H. Y. Sung, I. D. Williams and W. H. Leung, *Inorg. Chem.*, 2012, **51**, 3640-3647.